

University of Central Florida

STARS

Electronic Theses and Dissertations, 2020-

2022

Light Guiding and Concentrating using Self-Collimating Spatially-Variant Photonic Crystals

Chun Xia

University of Central Florida



Part of the [Electromagnetics and Photonics Commons](#)

Find similar works at: <https://stars.library.ucf.edu/etd2020>

University of Central Florida Libraries <http://library.ucf.edu>

This Doctoral Dissertation (Open Access) is brought to you for free and open access by STARS. It has been accepted for inclusion in Electronic Theses and Dissertations, 2020- by an authorized administrator of STARS. For more information, please contact STARS@ucf.edu.

STARS Citation

Xia, Chun, "Light Guiding and Concentrating using Self-Collimating Spatially-Variant Photonic Crystals" (2022). *Electronic Theses and Dissertations, 2020-*. 1700.

<https://stars.library.ucf.edu/etd2020/1700>

LIGHT GUIDING AND CONCENTRATING USING SELF-COLLIMATING SPATIALLY-VARIANT PHOTONIC CRYSTALS

by

CHUN XIA

B.S. Harbin Institute of Technology, 2015

M.S. University of Arizona, 2017

A dissertation submitted in partial fulfillment of the requirements
for the degree of Doctor of Philosophy
in College of Optics and Photonics, CREOL,
at the University of Central Florida
Orlando, Florida

Summer Term
2022

Major Professor: Stephen M. Kuebler

© 2022 Chun Xia

ABSTRACT

Advances in integrated photonic devices require low loss, easy-to-integrate solutions for chip-to-chip and chip-to-fiber interfacing. Among the most common solutions are traditional lenses. However, circular lenses require additional mounting mechanisms to ensure proper alignment. Additionally, the beam routing functionality cannot be added to the traditional lenses unless they are combined with mirrors and operate in the reflection mode. In this dissertation, we investigate lens-embedded photonic crystals (LEPCs) as a solution to flat and multifunctional lenses. The concept is demonstrated by creating self-collimating lattices containing a gradient refractive index lens (GRIN-LEPC), a binary-shaped lens (B-LEPC), and a Fresnel-type binary-shaped lens (F-B-LEPC). The devices are fabricated in a photopolymer by multi-photon lithography with the lattice spacing chosen for operation around the telecom wavelength of 1550 nm. Both the experimentally observed optical behaviors and simulations show that the device behaves like a thin lens, even though the device is considerably thick. The thickness of a B-LEPC was reduced threefold by wrapping phase in the style of a Fresnel lens. Embedding a faster-varying phase profile enables tighter focusing, and $NA = 0.59$ was demonstrated experimentally. Furthermore, we demonstrate experimentally that a Fresnel lens can also be combined into a bender, so one PC performs both bending and focusing functions, further reducing the footprint of the PC devices. We also explored a hexagonal lattice and demonstrated wide-angle and broadband self-collimation. The PCs are fabricated using the same material and method as that of the LEPCs. Optical characterization shows that the device strongly self-collimates light at near-infrared wavelengths that span from 1360 nm to 1610 nm. Self-collimation forces light to flow

along the extrusion-direction of the lattice without diffractive spreading, even when light couples into the device at high oblique angles. Numerical simulations corroborate the experimental findings.

This work is dedicated to my family and friends
for their love, support, and encouragement.

ACKNOWLEDGEMENTS

It has been a challenging yet rewarding journey to obtain a Ph.D. over the past short and long five years. I was able to achieve a great deal throughout the process, but none of it would have been possible without the assistance of many people, both personally and professionally.

As my supervisor, Dr. Kuebler has prepared me to be a Doctor of Philosophy through his great patience, continuous support, inspiring words, invaluable advice, and immense knowledge. He encourages me to dream big, but also reminds me that every step forward is equally as important. Also, I was continually challenged to step outside of my comfort zone and to take risks, but with a mitigation strategy. Additionally, I would like to thank Dr. Rumpf for his knowledge, experience, and discussions.

Besides my advisor, I would like to acknowledge my thesis committee, Dr. Peter Delfyett, Dr. Sasan Fathpour, Dr. Xiaoming Yu and Dr. Xun Gong, for their encouragement, insightful comments, and questions.

My sincere thanks go to my wonderful colleagues at the Nanophotonic and Material (NPM) group at the University of Central Florida: Rashi, Shaimum, Chad, Pooria, Alex, Geng, and Michael, and from the EM lab at the University of Texas at El Paso: Noel, Edgar, Jesus, and Manny. The experience of working with you had been enjoyable and rewarding. I also want to thank Boyang, Yingjie, Mengdi, Di and He for their support and advice on the experimental and characterization methods.

Further, I would like to thank Lawrence Lichtigfeld and the UCF Facilities team for their assistance in optimizing conditions in the fabrication lab, Robert Wong and Richard Zotti at the

machine shop for their assistance in making the custom parts, and CREOL staff Rachel Franzetta for her care and support.

Furthermore, I would like to express my gratitude to my parents, relatives, my girlfriend and her family for their wise counsel and sympathetic ear. I am grateful for all your support. Lastly, I would have been unable to complete this dissertation without the support of my badminton friends, Thomas, Katie, Khang, Hanson, Wen, Kevin, Calvin, Sam, and Adlynn, and finally, coach Hendry and his family, who provided stimulating conversations as well as happy distractions from my research.

TABLE OF CONTENTS

LIST OF FIGURES	xi
LIST OF ABBREVIATIONS	xviii
1. INTRODUCTION	1
1.1. Optical Interconnects	1
1.2. Multi-photon Lithography	3
1.3. Photonic Crystals	5
2. METHODOLOGY	10
2.1. Fabrication Method.....	10
2.2. Structural Characterization Method	15
2.3. Optical Characterization Method	16
3. WIDE-BAND SELF-COLLIMATION IN LOW REFRACTIVE INDEX HEXAGONAL LATTICE	18
3.1. Introduction.....	18
3.2. Unit Cell and Its Iso-Frequency Contour	20
3.3. Fabrication and Structural Characterization	22
3.4. Optical Characterization and Results	24
3.5. Summary	30
4. CYLINDRICAL-LENS-EMBEDDED PHOTONIC CRYSTAL BASED ON SELF- COLLIMATION	32
4.1. Introduction.....	32

4.2. Design of the lens-embedded spatially-variant photonic crystal	34
4.3. Fabrication and characterization	43
4.4. Modeling as a thin lens	51
4.5. Results and analysis	53
4.6. Summary	58
5. BINARY-LENS-EMBEDDED PHOTONIC CRYSTALS.....	60
5.1. Introduction.....	60
5.2. Design of the lens-embedded spatially-variant photonic crystal	61
5.3. Fabrication and structural characterization.....	64
5.4. Optical characterization results and analysis	65
5.5. Summary	71
6. LENSED-BENDER BASED ON SELF-COLLIMATING SPATIALLY-VARIANT PHOTONIC CRYSTALS.....	73
6.1. Introduction.....	73
6.2. Design a binary-lens embedded bender	74
6.3. Fabrication and structural characterization.....	81
6.4. Optical characterization results and analysis	84
6.5. Summary	88
7. SUMMARY AND OUTLOOK.....	90
APPENDIX A: COPYRIGHT PERMISSION LETTERS	93
APPENDIX B: PUBLIC RELEASEMENT STATEMENT	96
APPENDIX C: LIST OF PUBLICATIONS	98

REFERENCES	100
------------------	-----

LIST OF FIGURES

Figure 1.1: MPL processes. (I) Polymers near the focal region with intensity over the polymerization threshold will be polymerized. (II) Structures are fabricated by moving the focal spot along the pattern path. (III) The unexposed polymers will be developed to get the free-standing structure in (IV). Image taken from Danilevicius et al. [17].	4
Figure 1.2: (a) 3D band structure with iso-frequency planes slicing horizontally through the bands. (b) Cross-section projection onto the first Brillouin zone (FBZ). (c) Phase and energy flow direction extracted from the IFCs. Reprinted with permission from [34] © The Optical Society.....	6
Figure 1.3: Different optical effect due to the shapes of the IFCs. (a) The blue IFC has a sharp tip and will induce the super-prism effect. (b) The green IFC has a convex shape and will introduce negative refraction. (c) The yellow IFC is partially flat and can induce the SC effect. .	8
Figure 2.1: The experimental set-up for the MPL system used for patterning PCs.....	14
Figure 2.2: Zoomed-in view of the optical characterization system having the DF configured to be (a) parallel and (b) perpendicular to the SF.	17
Figure 3.1: (a) Unit cell of hexagonal PC consisting of cylindrical air-holes in a photopolymer background. (b) IFCs of the first seven bands with $kz = 0$ and wave vectors normalized to $2\pi c/a$. (c) Strength of SC for a range of PCs, shown as a contour plot of maximum deviation angle (in degrees) versus r/a and ωn . Reprinted with permission from [59] © The Optical Society.....	22

Figure 3.2: SEM images of a hexagonal PC with seven rows and seven columns of air holes and an extrusion length of 150 μm with targeted $r/a = 0.35$ and $a = 4.65 \mu\text{m}$. a) Side view and b) front views of the PC. Reprinted with permission from [59] © The Optical Society. 24

Figure 3.3: a) Schematic of the scanned-fiber system used to optically characterize the PCs. (c-e) Normalized intensity obtained by fiber-scanning at $\lambda_0 = 1550 \text{ nm}$ with b) no PC present and with the PC in the beam path oriented at angles c) $\theta_{\text{PC-fiber}} = 0^\circ$, d) $\theta_{\text{PC-fiber}} = 30^\circ$, and e) $\theta_{\text{PC-fiber}} = 50^\circ$. Reprinted with permission from [59] © The Optical Society. 25

Figure 3.4: Angular intensity distribution of light with PC positioned at different angles. The inset is an optical image of the PC positioned between SF and DF. Reprinted with permission from [59] © The Optical Society. 26

Figure 3.5: Beam divergence versus propagation distance with and without a PC between SF and DF. The top-, middle-, and bottom panels show data obtained for $\lambda_0 = 1360 \text{ nm}$, 1550 nm, and 1610 nm, respectively. The red trace shows how the beam diverges when freely propagating in air over 150 μm . The green, blue, and yellow traces show how the beam diverges after exiting the PC when $\theta_{\text{PC}} = 0^\circ$, 30° , and 50° , respectively. Reprinted with permission from [59] © The Optical Society. 29

Figure 4.1: (a) Cubic unit cell upon which the LE-SVPC is based. The red arrow indicates the direction light is incident. (b) Diagram illustrating the behavior of a LE-SVPC. The lattice is comprised of unit cells whose wall thicknesses are varied parabolically from the center to the side. (c1, d1) SEM images of two LE-SVPCs fabricated by multi-photon lithography (MPL). Each has a transverse-area of 71×71 unit cells, but they differ in length. The long LE-SVPC (left) has a

length along x of $Lx = 71$ unit cells. The short LE-SVPC (right) has $Lx = 35$ unit cells. Panels c2 - c3 and d2 - d3 show zoomed-in views of the two LE-SVPCs from the top and side with the sample tilted by 65° . Reprinted with permission from [16] © The Optical Society. 35

Figure 4.2: (a) A quadrant of the second TM band shown as one IFS at $\omega_n = 0.64$ and in-plane IFCs. (b) IFCs of the second TM band having $k_z = 0$. The IFC for $\omega_n = 0.64$ is indicated with the purple dashed line. Reprinted with permission from [16] © The Optical Society. 37

Figure 4.3: The shift of IFCs and change of mode profile for the second TM band at $\omega_n = 0.64$ as t/a varies from 0.24 to 0.40. (a) IFCs of the second TM band. Due to symmetry, only the second quadrant is drawn. The corresponding unit cells are shown at the right. The red dashed line indicates an xy -plane in which E_z is evaluated. (b-f) The real part of the eigenmodes calculated using PWEM. (g-k) Propagation of Bloch modes over four periods, calculated using FDTD. The light grey background shows the structure of the lattice within the xy -plane. Reprinted with permission from [16] © The Optical Society. 38

Figure 4.4: Relationship between t/a and n_{eff} extracted from FDTD (*yellow cross*) and PWEM (*red dot*) simulations for the TM mode. Reprinted with permission from [16] © The Optical Society..... 42

Figure 4.5: Profile of wall-thickness t across the LE-SVPC (parallel to y) shown in Figure 4.1c(1). Measured values of t are plotted as black dots. The solid red line shows a fit of the measurements to a second-order polynomial. The error bars represent the ± 1 standard deviation of five measurements. Reprinted with permission from [16] © The Optical Society. 46

Figure 4.6: Optical characterization of two LE-SVPCs like those shown in Figs. 4.1c(1) and 4.1d(1), having (*left*) $L_x = 71$ unit cells and (*column*) $L_x = 35$ unit cells, and measured with $d_1 = 150 \mu\text{m}$. Panels (a3) and (b3) are xy -scans that show how the transverse beam profile changes along y when light exits the LE-SVPC and propagates distance x . These data were used to obtain the width of the scan-profiles as FWHM versus x , shown in (a4) and (b4). Green dashed lines identify focal points $d_2 = x$, where the beam is narrowest along y and where FWHM_{\min} is located. At these points, full transverse scans of the beam profile appear as seen in (a1) and (b1). For comparison (a2) and (b2) show transverse profiles recorded without the LE-SVPC present. When the LE-SVPC is present, the beam narrows in the horizontal plane, showing the device behaves like a cylindrical lens, and the focal power is stronger for the longer LE-SVPC. Reprinted with permission from [16] © The Optical Society. 50

Figure 4.7: Optical modeling and characterization of focusing by LE-SVPCs. (a) Schematic of the model. Light emanates from a single-mode optical fiber (SF) as a Gaussian beam of width w_{01} , propagates distance d_1 , then couples into the LE-SVPC, which is treated as a thin lens. SC forces light to travel the length of the device without spreading or focusing, even as it accumulates a quadratic phase profile. Upon exiting, the light focuses to a Gaussian beam of width w_{02} after propagating distance d_2 . Because SC prevents the beam width from changing within the LE-SVPC, it can be treated as a thin lens. (b) Experimental measurements of FWHM as a function of distance x when $d_1 = 50 \mu\text{m}$, $75 \mu\text{m}$, $100 \mu\text{m}$, and $150 \mu\text{m}$, after passing through the long LE-SVPC, like that in Figure 4.1(c1). (c) Experimental and simulated change of d_2 and FWHM_{\min} for a long LE-SVPC as a function of d_1 , with vertically (z) and horizontally (y)

polarized light. The shaded region shows how d_2 and FWHM_{\min} vary in simulation when f changes by $\pm 5 \mu\text{m}$. Reprinted with permission from [16] © The Optical Society. 52

Figure 5.1: Binary-lens-embedded PC. (a) Unit cell. (b) Design of lattice. Inside (yellow) and outside (pink) the lens region, t is thick and thin, respectively. (c - e) SEM images of a B-LEPC having $71 \times 71 \times 71$ unit cells. (d) Top-view of walls transitioning from thick to thin. (e) Side-view of elliptical rods. Light is incident along the red arrow. 61

Figure 5.2: Optical characterization of B-LEPC seen in Figure 5.1(c). (a) xy -scan obtained with z -polarized light and $d_1 = 150 \mu\text{m}$. (b) FWHM versus x extracted from xy -scan. The focus and FWHM_{\min} appear at $x = d_2$ (*blue dashed line*) (c, d) Beam profiles obtained from yz -scans at $x = d_2$ with and without B-LEPC. (e) FWHM_{\min} and d_2 plotted versus d_1 for z - and y -polarized light. Black curves and shaded regions give simulated FWHM_{\min} and d_2 for $f = 90 \mu\text{m} \pm 5 \mu\text{m}$ 66

Figure 5.3: Fresnel B-LEPCs designed to have identical *physical* length L_0 but increasingly faster phase wrapping for tighter focusing. Without phase wrapping, the *effective* length of the lensing region (Lx) is (#1) $71a$, (#2) $1.5 \times 71a$, and (#3) $2 \times 71a$. (a1 - a3) SEM images of the F-B-LEPCs. (b1 - b3) xy -scans with $d_1 = 150 \mu\text{m}$ and z -polarized light. Dashed blue lines indicate the apparent focus at $x = d_2$. (c1 - c3, d1 - d3) Transverse scans in the focal plane with and without the F-B-LEPC. (e1 - e3) FWHM_{\min} (*orange*) and d_2 (*blue*) plotted versus d_1 for z - and y -polarized light. Note the change in scale of the vertical axes. 69

Figure 5.4: Simulation of a Gaussian beam coupled into a F-B-LEPC. (a) The structure's geometry matches the fabricated device in Figure 5.3(a1). (b) E_z -field in region identified with green-dashed line. (c) Normalized irradiance as $|E_z|^2$ within and after exiting the PC. 71

Figure 6.1: Design a (c) lensed bender by combining (a) a bender and (b) a lens.....	74
Figure 6.2: (a) The 3D unit cell consists of an elliptical rod intercepting a wall. The two parameters that need to be spatially varied are t and $2r_1$, which are translated into (b) H- and (c) V-bar, separately, which are then used to compose a (d) 2D unit cell for spatial variation.	75
Figure 6.3: Gray-scale unit cells and the maps for generating a 90° bend. (a1) and (b1) are gray scale unit cells for a H- and V-bar, respectively. a(2-4) and b(2-4) are two sets of input maps containing period, angle, and fill-factor for separately spatially vary the H- and V-bar. The generated analogue and binary SVLs containing 11×11 unit cells generated from the H- and V-bar are shown in (c1) and (c2), and (d1) and (d2), respectively. (e) Synthesized lattice from combining (c2) and (d2).....	76
Figure 6.4: Translating a lens profile from embedding inside of (a) a normal lattice to inside of (b) a bender	79
Figure 6.5: Center (solid) and contour (dash) lines of the (a1) H-bars and (a2) V-bars. Grouped points that define coordinates for the (b1) H- and (b2) V-bars. The points are where the central lines of the H- and V-bar cross.	80
Figure 6.6: SEM images of a bender having $71 \times 71 \times 71$ unit cells. (a) Side-view of the whole lattice. Zoomed-in top view at the (b) middle and the exit side of the lattice. Light is chosen to incident along the direction of the red arrow.....	82
Figure 6.7: SEM images of a lensed-bender having $71 \times 71 \times 71$ unit cells. (a) Side-view of the whole lattice. Zoomed-in view from the (b) top and the (side). Light is chosen to incident along the direction of the red arrow.....	83

Figure 6.8: Optical characterization of the bender seen in Figure 6.6(a). a(1-4) are optical microscope images when the SF is scanned from the bottom to the top of the lensed-bender along the y -axis, with the step size of $20\text{ }\mu\text{m}$ and $d1 = 100\text{ }\mu\text{m}$. The xy -scans of the SF at those locations are shown in b(1-4) and d(1-4) for the z - and y -polarized light, respectively. The FWHM at each y -location is extracted from b(1-4) and d(1-4), and are shown in c(1-4) and e(1-4), respectively. 85

Figure 6.10: Optical characterization of the lensed-bender seen in Figure 6.6(a). a(1-5) are optical microscope images when $d1$ is set to $50\text{ }\mu\text{m}$, $100\text{ }\mu\text{m}$, $150\text{ }\mu\text{m}$, $200\text{ }\mu\text{m}$, and $250\text{ }\mu\text{m}$. At these $d1$ locations, the xy -scans are shown in b(1-5) and d(1-5) for the z - and y -polarized light, respectively. The FWHM at each y -location is extracted from b(1-5) and d(1-5), and are shown in c(1-5) and e(1-5), respectively. 86

Figure 6.11: Detection of light not bent through the bender. (a) The DF is scanned from -30° to 10° with the step size of 5° when $d1$ is set to $250\text{ }\mu\text{m}$. (b) Maximum signal strength versus the rotation angle. The blue line is a reference for light bent by 90° 87

LIST OF ABBREVIATIONS

1D	One-dimensional
2D	Two-dimensional
3D	Three-dimensional
AOM	Acousto-optic modulator
BZ	Brillouin zone
BOE	Buffered-oxide etch
DI	De-ionized
DF	Detection fiber
FDTD	Finite-difference time-domain
FDFD	Finite-difference frequency-domain
FBW	Frequency bandwidth
FBZ	First Brillouin zone
GRIN	Graded-index
IFC	Iso-frequency contour
IFS	Iso-frequency surface
IPA	Isopropyl alcohol
LEPC	Lens-embedded photonic crystal
MPL	Multi-photon lithography
NA	Numerical aperture
OPG	Optical parametric generators

PC	Photonic crystal
PWEM	Planewave expansion method
PML	Perfectly matched layer
PD	Photodiode
PGMEA	Propylene glycol methyl ether acetate
SF	Source fiber
SEM	Scanning electron microscope
SVPC	Spatially-variant photonic crystal
SVL	Spatially-variant lattice
SC	Self-collimation
SVPC	Spatially-variant photonic crystal
SVL	Spatially-variant lattice

1. INTRODUCTION

1.1. Optical Interconnects

The way human beings transfer information has been revolutionized by many inventions, the two prominent ones being optical fibers and the transistors. In long-haul communications, traditional electrical transmission has been replaced by optical fibers due to its high bandwidth, low cross talk, and exceptionally low loss. To match up with the increase of data transportation speed and capacity in long haul communication, optics-based transceivers are also replacing metal transceivers in board-to-board, backplane, and chip-to-chip applications in short distance communication [1]. Combining with the breakthroughs of fabricating semiconductors with 10 nm [2] and 7 nm [3] features, more transistors on integrated circuits (ICs) enables optoelectronics with more functions, lower cost, and higher efficiency.

The growth in communication speed also boosts the amount of Internet Protocol (IP) traffic. As predicted by Cisco Report, global IP traffic is expected to reach 4.7 zettabytes of traffic per year by 2022 [4]. These data are transported through millions of servers, and thousands of datacenters connected with racks of optical instruments and are still growing in scale. Depending on the nature of applications, some traffic flows in and out of data center (DC) while some stays internal to the DC. For some applications in Facebook and Google, the internal traffic dominates and often requires computation of data from multiple servers [5]. One of the key components in DCs is optical fiber-based transceivers. And the datacenters are interconnected with optical fibers, which consumes relatively high power and is bulky, complicated, and hard to manage architecture

upgrade and system scalability [6]. The dense cabling also decreases heat dissipation by obstructing airflow and increases cable cost as reported from HP [7].

An alternative solution to reducing the complexity of cabling issues is to use free-space optical (FSO) communication interconnects [8]. The challenge is, however, to have beam routing elements that can convert difference in beam sizes and shapes between single-mode fibers and on-chip lasers. One approach involves the edge-coupling method using gratings, such as coupling single-mode fibers to InP-based lasers [9]. A second approach is to create micro-lenses and attach them to the facets of fibers and chips [10]. Both methods require precise alignment with tight tolerances. The additional etching and polishing processes required when preparing gratings and waveguide edges also complicate the fabrication process. Recent advances in the patterning of beam-shaping optics using in-situ multi-photon lithography have shown promise in overcoming these limitations [11]. Using 3D printing, optics of virtually any shape can be printed, such as mirrors, prisms, lenses, axicons, and gratings. With this low-cost and on-demand approach, coupling between problems becomes much more adaptable and flexible.

This thesis explores a new solution to address the optical interconnect problem using the photonic crystal (PC) approach. As light travels inside PCs, the power flow and phase can be independently controlled, and this concept is applied to make optical devices such as lenses and benders. Chapter 3 describes a 3D hexagonal lattice is capable of transmitting light without diffraction. In Chapter 4 and Chapter 5, we demonstrate the possibility of constructing lenses inside PCs by spatially varying the lattice fill-factor. Shape profiles of the lens include a graded-index lens, a binary lens, and a Fresnel lens. Chapter 6 shows a lensed bender that performs two optical functions in one device. A lensed bender can gradually bend the direction of light flow by

90 degrees, and it also functions as a lens, so light focuses once it leaves the PC. The sections below describe the fundamental concepts necessary to understand the work presented in this thesis.

1.2. Multi-photon Lithography

Fabricating 3D nanostructures is an active area of research. Along with the trend of device miniaturization and integration, various fabrication techniques were put forward, such as electron beam lithography [12], self-assembly [13], micro-stereolithography [14] and deep UV lithography [15]. However, these techniques are expensive, and only applicable to certain 3D designs with less complexity.

Multi-photon lithography (MPL) is a layer-by-layer fabrication technique that mainly utilizes the two-photon polymerization (TPP) process [16]. It offers the possibility of fabricating potentially arbitrary shaped 3D structures with resolution down to 100 nm and the scanning speed ranges from $100 \mu\text{m s}^{-1}$ to 10 mm s^{-1} , without needing photomasks. MPL has numerous applications in optics and photonics, micromachines, regenerative medicine and biomedical engineering.

The photo-polymerization process has three basic steps: initiation, chain propagation and chain termination. In the initiation process, photo-initiators absorb two photons and generate radicals. The radicals will combine with monomers to form long polymerization chains and will be terminated once another radical is combined on the other end. Polymerization begins when the radical concentration exceeds a certain threshold due to radical quenches in the resin. The radical concentration threshold can be directly translated into laser irradiance threshold. Features will form

at where the irradiance is no less than the threshold intensity. Such threshold is hard to reach due to the low absorption cross-section of TPP. MPL only becomes reasonably efficient when high intensity laser pulses are used to increase the rate of multiphoton absorption. Intensity is increased in time by using femtosecond pulses and in space by tightly focusing the pulses into the material. A typical combination of the laser parameters is 10 mW for laser power, 100 fs for the pulse duration, 100 MHz for the repetition rate, and the focal spot size of $0.1 \mu\text{m}^2$, which yields the intensity of 10^{12} W/cm^2 and the flux density of $10^{31} \text{ photons s}^{-1} \text{ cm}^{-2}$.

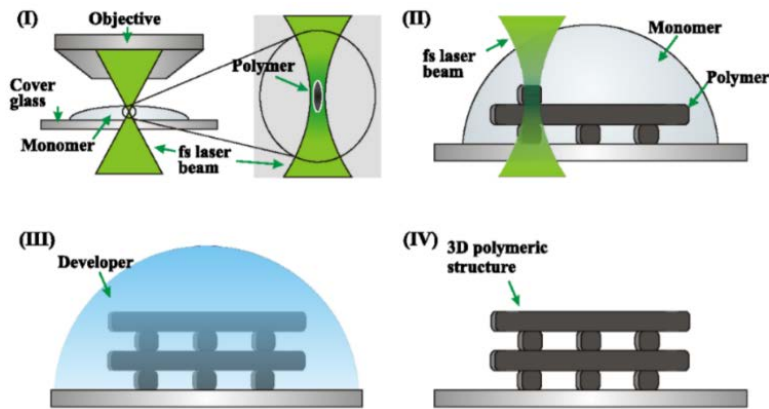


Figure 1.1: MPL processes. (I) Polymers near the focal region with intensity over the polymerization threshold will be polymerized. (II) Structures are fabricated by moving the focal spot along the pattern path. (III) The unexposed polymers will be developed to get the free-standing structure in (IV). Image taken from Danilevicius et al. [17].

The resolution of the system depends on the focusing spot size and the polymerization threshold. As shown in Figure 1.1, complex 3D structures can be formed by scanning the focus spot throughout the photopolymer along the path of a targeted pattern. The unexposed resin is

dissolved by immersing the sample in development solvents, thus leaving behind the exposed region on the substrate.

1.3. Photonic Crystals

Photonic crystals (PCs) are periodic materials [18, 19] that are structured to control photons, analogous to how semiconductors control electrons [20, 21]. PCs were first studied by Rayleigh as early as 1887, but the concept of PCs was not put forward until over a century later, after two ground-breaking papers in 1987 from John and Yablonovitch [22, 23]. In 1996, a 2D PC was first demonstrated to operate at optical wavelengths in semiconductor materials [24].

PCs have broad application in integrated photonics because of their diverse properties. PCs offer abundant opportunities for controlling the dispersion and propagation of light through the choice of materials, lattice symmetries, and geometry of the repeated unit cell.

The properties of PCs can be understood by examining the photonic bands and dispersion surfaces [25]. Strategies employing PCs can be divided into in-bandgap and out-of-bandgap applications. With in-bandgap applications, such as slab waveguides [26] and optical fibers [27], light is forced to propagate along defect-paths within the lattice. Significant effort has focused on understanding how to increase and control the width of photonic bandgaps [28, 29]. Out-of-bandgap applications exploit the spatial dispersion of allowed modes. Spatial dispersion can be understood by examining the shape of photonic bands and the corresponding iso-frequency contours (IFCs).

The link between the shape of an IFC and power flow is

$$\mathbf{v}_g(\mathbf{k}) = \nabla \omega(\mathbf{k}), \quad (1.1)$$

which indicates optical power flows in a direction that is normal to the IFC surface. The shape of the IFCs gives rise to novel effects including negative refraction [30], slow-light [31], superprism effect [32], and self-collimation (SC) [33].

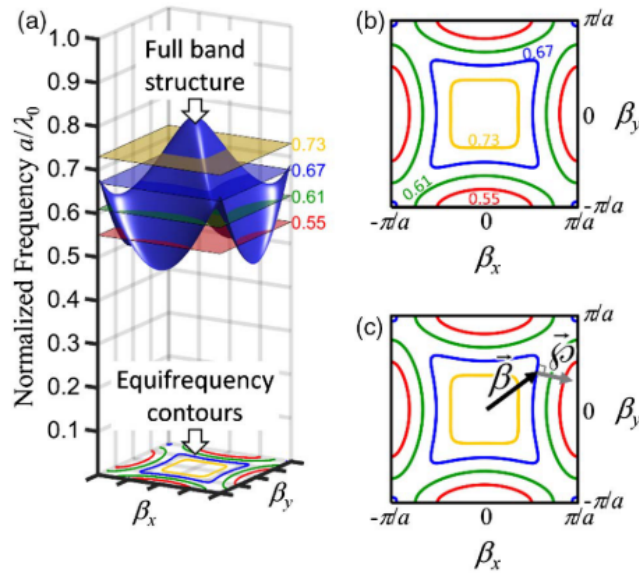


Figure 1.2: (a) 3D band structure with iso-frequency planes slicing horizontally through the bands. (b) Cross-section projection onto the first Brillouin zone (FBZ). (c) Phase and energy flow direction extracted from the IFCs. Reprinted with permission from [34] © The Optical Society.

The behavior of light allowed to propagate inside of PCs can be predicted using the planewave-expansion method (PWEM) which reformulates and solves the Maxwell's equations as an eigen value and eigen vector problem [25]. The eigen values are expressed in normalized

frequency $\omega_n = \omega a / 2\pi c = a / \lambda_0$ ("reduced frequency" [35]), where ω is angular frequency of the light, and λ_0 is vacuum wavelength, and the eigen vectors of the modes allowed to propagate inside of the lattice. The spatial dispersion of a uniform lattice composed with a given unit can be fully understood by examining its band diagram that can be formed by solving a range of wavevectors in the first Brillouin zone (FBZ) and arranging their eigenvalues vertically.

The spatial dispersion of a PC can be visualized by examining the shape of its photonic bands and the corresponding iso-frequency contours (IFCs). IFCs are the cross-sections between photonic bands and an iso-frequency plane. For example, Figure 1.2(a) shows the three-dimensional (3D) band diagram of a certain band having wavevectors β_x and β_y spanning across the first Brillouin zone and its IFCs are shown in Figure 1.2 (b). The red IFC at $\omega_n = 0.55$ in Figure 1.2 (b) is constructed by first creating an iso-frequency plane at $\omega_n = 0.55$ and then projecting the shape where it intersects the band of interest to the bottom. The IFCs at other frequencies are formed by repeating this process until all the frequencies within the band of interest are examined.

The link between the shape of an IFC and the direction energy flows is described by Eq. 1.1, which can be interpreted to mean that optical power flows in a direction that is normal to the IFC surface. For example, the Bloch wave vector $\vec{\beta}$ drawn from the origin of the IFC plane to the blue IFC in Figure 1.2(c) describes how phase advances inside of lattice at $\omega_n = 0.55$. The direction of power flow of the Poynting vector \vec{P} is drawn from the tip of $\vec{\beta}$ along the local surface normal direction. For normal dispersion, the \vec{P} points towards the outside of the surface normal while abnormal dispersion the inside of the surface normal. As an example, the blue, green, and yellow

IFC shown in Figure 1.3 a, b and c, respectively, will introduce the super-prism effect, negative refraction and the SC effect.

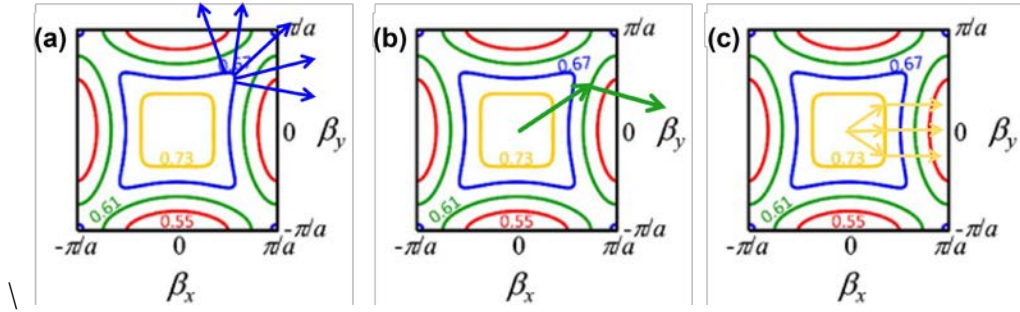


Figure 1.3: Different optical effect due to the shapes of the IFCs. (a) The blue IFC has a sharp tip and will induce the super-prism effect. (b) The green IFC has a convex shape and will introduce negative refraction. (c) The yellow IFC is partially flat and can induce the SC effect.

1.3.1. Self-collimation Effect

Controlling light without loss to beam spreading is essential in photonics. SC is one of the candidates that enables light to propagate without diffraction. SC happens where flat IFCs occur. SC was first experimentally observed by Kosaka and Wu [33, 36] who showed that light can propagate inside of a PC without diffraction. With the development of the technique, the beam propagation inside of the lattice was detected and mapped out at microwave frequencies by scanning a monopole inside 2D and 3D PCs [37, 38] and at optical frequencies using near-field scanning optical microscopy to image light scattering out of a 2D PC [39, 40]. The experiments proved that SC enables light propagation inside of a lattice without diffraction even for distance

of millimeter scale at the optical wavelength. Other 2D and 3D devices that exploit SC have been fabricated in silicon, such as PC waveguides [41] and beam splitters [42].

2. METHODOLOGY

The workflow of studying the behavior of functional devices based on spatially-variant photonic crystals (SVPCs) involves three key steps. First, a suitable unit cell is selected, and its dimensional parameters are optimized for a strong SC and ease of fabrication. Second, PCs based on such unit cell are fabricated using our in-house MPL system. Third, the structural properties of the fabricated PCs are verified using SEM and optically properties are determined using a fiber-scanning optical characterization system. Next, the results will be analyzed and fed into electromagnetic simulation tools to generate new understandings and to optimize the design.

2.1. Fabrication Method

2.1.1. Sample Preparation

Preparation of the substrate for MPL begins with the removal of particles and chemical impurities, followed by the heating process for the removal of water and a treatment with an adhesion promoter.

In the sample cleaning step, Microscope glass slides (thermo-scientific) are cut into 5 mm \times 5 mm pieces for use as substrates. To remove organic impurities and particles from the substrates, the following procedure was followed:

1. Sonicate in 1 M aqueous potassium hydroxide at 60° for 30 minutes.
2. Serially dilute and rinse with deionized water (DI)
3. Dry in air

As the next step, the substrates will be stored in an oven at 100° to prevent water molecules from absorbing on surfaces exposed to air humidity and to improve surface adhesion.

When fabricated with MPL, structures with a high aspect ratio have poor adhesion to cleaned bare glass substrates and will easily detach if handled carelessly during their transfer. An adhesion promoter layer can modify the substrate surface and enhance adhesion. Using the following procedures, the adhesion promoter layer was coated on a glass substrate:

1. Prepare a 1 vol-% solution of (3-acryloxypropyl) trimethoxysilane (APTMS, CAS# 4369-14-6) in methanol
2. Place substrate on spin-coater chuck
3. Flood surface of substrate with 1 vol-% solution of APTMS in methanol and spin coat with the recipe in Table 2.1
4. Transfer samples to hot plate and bake at 90 °C for 30 s
5. Transfer sample back to spin-coater and repeat steps 3-4 three times

After the substrates have cooled, they will be transferred into a clean disposable petri dish for storage.

Table 2.1. Spin coat recipe for coating adhesion promoter

<i>Step no.</i>	<i>Ramp-time / s</i>	<i>Revolutions / min</i>	<i>Dwell time / s</i>
<i>0</i>	<i>0</i>	<i>0</i>	<i>0</i>
<i>1</i>	<i>5</i>	<i>2500</i>	<i>30</i>
<i>2</i>	<i>500</i>	<i>0</i>	<i>0</i>

2.1.2. Photopolymer IP-Dip

IP-Dip is a commercialized resin from Nanoscribe. IP-Dip is acrylate based and offers fast polymerizing, rigid structures, and the highest resolution among the commercial resins. IP-Dip is intensively used in dip-in laser lithography in which the tight focusing objective lens is in contact with the resin to index-match, reduce aberration due to interface [46], and increase resolution.

The major components can be found on the published MSDS information and include 2-(hydroxymethyl)-2-[[1-oxoallyl]oxymethyl]-1,3 propanediyl diacrylate (trimethylolpropane triacrylate, TMPTA), 2-(2-phenylphenoxy)ethyl prop-2-enoate (B), H-fluorene-9,9-diylbis(4,1-phenyleneox-yethane-2,1-diyl)bisacrylat (C), and 7-diethylamino-3-thenoylcoumarin (D) [47]. TMPTA is a common trifunctional acrylate ester monomer that serves as the cross-linking agent during polymerization. Reactant B and C are also monomers and copolymerize under polymerization. The biphenyl structures in B and the fluorene structure in difunctional monomer C serves another function to raise the index of refraction of the resin to that of the last optic of the objective lens. D is an efficient radical type photoinitiator. It has been suggested that C may also function as a photosensitizer during photoreaction due to the fluorene derivatives [48]. The composition has high viscosity and therefore permit unobstructed movement of the lens.

The refractive index of the polymerized photopolymer “IP-Dip” in the ultraviolet (UV) to near-infrared (NIR) wavelength range has been measured in [49, 50]. They report that at the telecom wavelength, such as 1550 nm, the polymerized “IP-Dip” has a refractive index of 1.525, and the absorption is negligible.

2.1.3. Fabrication of PCs using Multi-Photon Lithography

The experimental set-up for fabricating PCs with MPL is shown in Figure 2.1. The light source is a mode-locked Ti:Sapphire laser (Coherent-Mira) that generates pulses with a duration of 120 fs at 76 MHz. The light will first go through an acousto-optic modulator (AOM, Gooch and Housego) for intensity modulation. Then, light will be reflected by Mirror 1 (M1) to a telescope system for beam amplification. The telescope system is composed with lenses having focal lengths of -50 mm and 200 mm, respectively, and the beam diameter will be amplified by four times after passing through the telescope system. The amplified beam is then routed by Mirror 2 (M2) to overfill the back aperture of the objective lens (Nikon Type A oil, 60 \times , 1.4 NA). The objective lens tight focuses the beam into photopolymer to induce photopolymerization starting from the surface of a glass sample. Two clamps are used to attach glass substrates to a sample holder. This sample holder is then mounted onto a three-axis nano-positioner (Physik Instrumente), which will then be moved around for patterning.

A successful fabrication requires three steps. 1) Power calibration: The lasing power varies each time the source laser is turned on and off. Before each fabrication, the average power after the objective lens was measured with a calibrated integrating sphere (Optronic Laboratory 731). This step enables correct measurement of the power required for fabrication and is vital for structure repeatability. 2) Finding the interface between photopolymer and the glass substrate: This procedure is called leveling. A failure to level will result in structures being patterned above the glass substrates and being washed away during the post development process. To ensure structures are adhered to the substrate, fabrication must start with the focal spot at or below the interface.

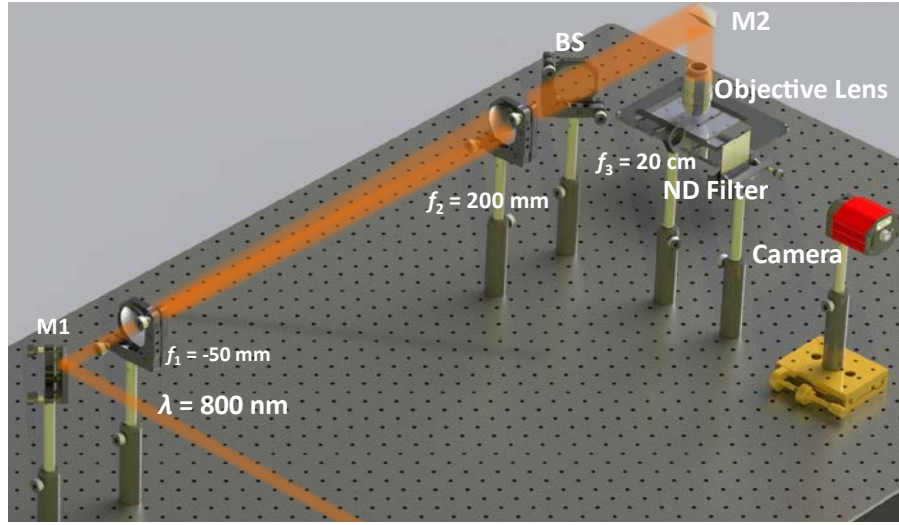


Figure 2.1: The experimental set-up for the MPL system used for patterning PCs.

The surface of the sample glass is located using fluorescence light recollected by the objective lens and imaged by a CCD camera placed on the conjugated plane of the objective lens' focal plane. Initially, the sample is below the focal spot. The fluorescence spot is always present when the focal point is above the glass sample. As the sample is moved across the focal point, the fluorescence spot will gradually weaken and eventually disappear. This is because the fluorescence spot is focused within the glass sample. Glass samples are leveled at the point where the fluorescence disappears completely. The leveling procedure is repeated when the stage is moved to another two locations along the transverse plane. Using the coordinates of the three leveling points, the angle between the glass sample and the optical axis of light after the objective lens will be calculated. This angle is used to rotate the input structure so that the fabricated structure is perpendicular to the glass substrate. Finally, the focus was buried 3 μm to ensure good adhesion.

3) Loading fabrication file: The fabrication file contains coordinates, power, and speed for lines or

arcs that define the structure. The fabrication process was fully automated using a LabView program. It coordinates the stage to move along the desired path with the given speed while simultaneously controlling power by sending needed voltage to AOM based on the input file. An array of short pillars is added in the write-file, so the fabricated structure can shrink isotropically during development. A support tower is also added to raise the whole structure up by 120 μm , allowing free movement of the SF and DF for optical characterization.

2.1.4. Post Development and Optical Inspections

After fabrication, samples are disassembled and transferred to a development funnel for post development. During the development process, the unexposed photoresist must be washed away, leaving only the exposed structure. A control valve on the funnel allows the solvent to be contained or drained. Before adding development solvents, PGMEA is rinsed to clean the inner side of the funnel. Structures were developed by immersing sequentially in PGMEA three times for thirty minutes each, IPA, and DI water for five minutes, then draining and allowing them to dry in the air. The funnel is filled with development solvents with the valve closed, and the sample is soaked and drained before a new type of solvent is added.

2.2. Structural Characterization Method

Structural properties of the fabricated structures were obtained and accessed using scanning electron microscopy (SEM, ZEISS ULTRA-55). SEM images give useful information such as the feature dimensions, shrinkage levels, and completeness of development. SEM images samples by

using electrons and can achieve sub-nanometer resolution, which cannot be achieved using traditional optical imaging techniques. In SEM, the electron beam is scanned over a raster-scanning pattern, and the position of the beam combined with the detected signal is used to create an image.

The samples must be sputter-coated before being placed in the high vacuum chamber for SEM imaging. The samples fabricated with MPL are polymer-based and are not conductive. During sputter coating, a thin layer of conductive material is applied to non-conducting specimens. By doing this, charges are prevented from building up under the electron beam. In our applications, all samples are sputtered with gold (Emitech K550) for 90 s at each of two angles, which are both tilted at 50°.

2.3. Optical Characterization Method

Prior to SEM imaging, structures were optically characterized using a scanned-fiber system. The light source consists of a femtosecond laser amplifier (Coherent Legend) pumping two optical parametric generators (OPGs). The signal beam (pulse duration ~ 120 fs, bandwidth ~ 30 nm) was used to characterize the PCs at $\lambda_0 = 1360 \text{ nm} - 1610 \text{ nm}$. Laser pulses were directed through a 10/90 cube beam splitter. The weaker beam was directed onto reference detector DET1 (Thorlabs PDA20H). The stronger beam passed through a polarizer and half-wave plate combination for polarization control and was then coupled into a source fiber (SF) using an objective lens. The opposite end of SF was positioned at the entrance face of the PC, as shown in Figure 2.2. Light exiting SF propagated through the PC and was collected with detection fiber DF

connected to signal detector DET2 (Thorlabs PDA20H). Both the SF and DF were mounted on rotational stages for angular measurements. To prevent SF and DF (Thorlabs 1550 BHP, single mode, $NA = 0.13$) from dragging on the substrate, the ends near the PC were reduced in diameter to $30\text{ }\mu\text{m}$ using buffered-oxide etch (J.T. Baker 1178-03). The tips of SF and DF near the PC were mounted on separate rotation- and xyz -translation stages so that the light intensity could be measured as a function of angle and position. Signals of the infrared detectors were connected to an oscilloscope (Tektronix TDS 2014). Data acquisition was automated using LabView. To reduce shot-to-shot noise, the signal from DET2 (I_{sig}) was referenced to that from DET1 (I_{ref}).

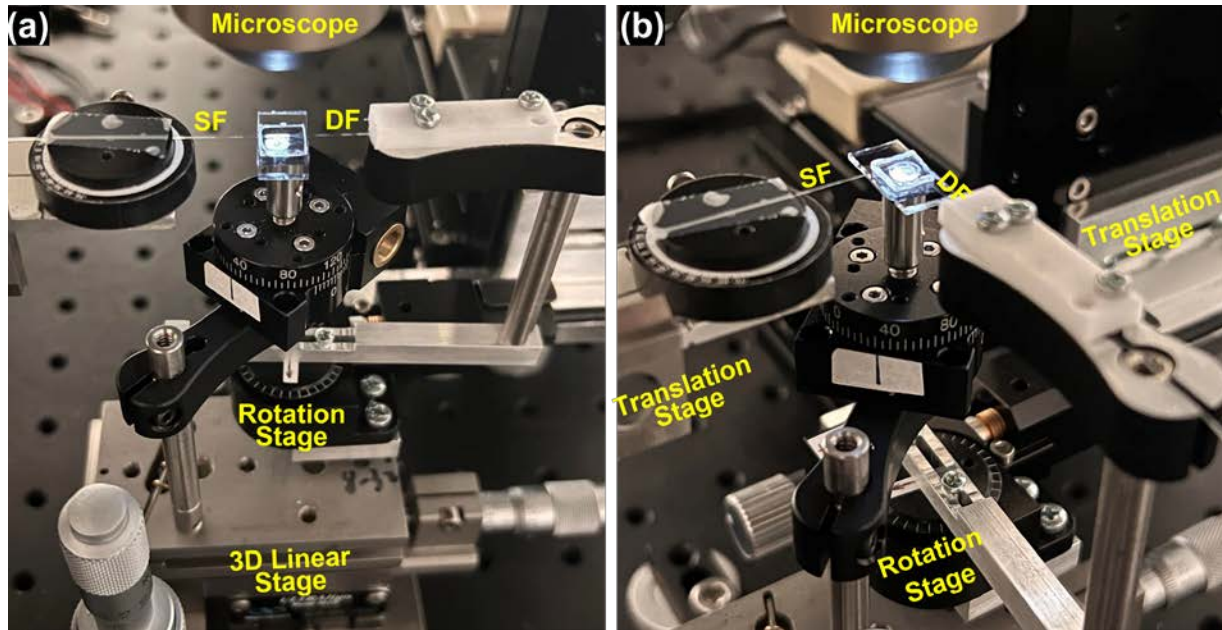


Figure 2.2: Zoomed-in view of the optical characterization system having the DF configured to be (a) parallel and (b) perpendicular to the SF.

3. WIDE-BAND SELF-COLLIMATION IN LOW REFRACTIVE INDEX HEXAGONAL LATTICE

Authored by Chun Xia, Stephen Kuebler, Noel Martinez, Manuel Martinez, Raymond Rumpf, and Jimmy Touma, the content of this chapter has been published in Optics Letters on April 29th, 2021.

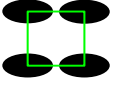
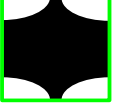
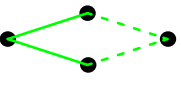

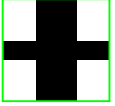
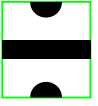

3.1. Introduction

Controlling light without loss to beam spreading is essential in photonics. SC can be used to mold the flow of light, without divergence. Two- (2D) and three-dimensional (3D) devices that exploit SC have been fabricated in silicon, such as PC waveguides [41] and beam splitters [42]. Various geometries have been studied to improve SC and bandwidth in high-index lattices ($n > 3$).

The SC effect was experimentally observed by Kosaka and Wu [33, 36]. SC has been detected at microwave frequencies by scanning a monopole inside 2D and 3D PCs [37, 38] and at optical frequencies using near-field scanning optical microscopy to image light scattering out of a 2D PC [39, 40]. These methods are not well suited for studying SC within a 3D volumetric PC operating at telecommunication wavelengths. Table 3.1 summarizes unit cells in literature having FBW bigger than 10% and offer SC. All the listed unit cells are based on materials with the effective index bigger than 3. To date, there are few studies of SC involving 3D PCs in low-index materials ($n \sim 1.5$) [51], and none exploring situations in which an input beam is incident at large oblique angles at optical wavelengths.

This chapter reports optical-wavelength, wide-angle, broad-band SC in a 3D PC fabricated in a low-refractive-index photopolymer. The device (Figure 3.1a) is a hexagonal array of cylindrical air-holes having radius r and periodicity a within a block of photopolymer. There are no intended defects, such as filled-in-, displaced-, or misshapen features. Energy flows parallel to the cylinders, but not necessarily within them, directed by SC. As a result, the hexagonal PC differs from 1) waveguides that operate through antiresonance and lack periodicity along the transverse plane [52] and 2) holey fibers which guide light only along the defect paths [27].

Table 3.1: Unit cells in literature with the FBW bigger than 10%

Unit cell	Mode	SC band	θ_A	FBW	Index	Ref.
 2D Elliptical rods	TM	4	$< 90^\circ$	10.9%	$\varepsilon = 11.56$	[53]
 2D Elliptical holes	TE	4	$< 90^\circ$	9%	$\varepsilon = 11.56$	[53]
 2D Rhombus lattice	TM	3	$< 90^\circ$	17%	$n = 3.5$	[43]
 2D Complex Rhombus lattice	TM	5	$< 90^\circ$	17%	$\varepsilon = 12$	[54]
 2D Rectangular	TE & TM	2	$< 25^\circ$	15%	$\varepsilon = 12$	[55]
 2D hybrid rod and wall	TM	4	$< 90^\circ$	13%	$n = 3.5$	[56]
 3D air holes in the hexagonal lattice	TE & TM	1-6	$< 90^\circ$	42%	$\varepsilon = 12$	[54]

To explore SC of the hexagonal PC, devices were fabricated by multiphoton lithography (MPL), characterized structurally and optically, and analyzed against simulations.

3.2. Unit Cell and Its Iso-Frequency Contour

The allowed modes were computed with a 3D frequency-domain eigenmode solver [57] for several r/a . Eigenvalues are expressed in normalized frequency $\omega_n = \omega a / 2\pi c = a / \lambda_0$ ("reduced frequency" [35]), where ω is angular frequency of the light, and λ_0 is vacuum wavelength. Figure 3.1(b) shows the first seven bands for $r/a = 0.40$, the vertical in-plane wavevector $k_z = 0$, and $k_x = 0 - 6$, in units of $2\pi/a$. The first seven bands are considered because they are closely spaced in ω_n , and light may couple into any of these. The colored lines represent IFCs with ω_n varying from 0.5 to 4.0 in steps of 0.5.

Inspecting the first seven bands, arranged from left to right in Figure 3.1(b), one sees the IFCs become flatter as ω_n increases. Many prior reports of SC involve lattices for which the IFCs "invert," changing in profile from concave to convex versus ω_n , with a narrow region of SC in between. But inversion is not essential for SC because it occurs where IFCs are flat, with [42] or without [43] inversion. The IFCs of the hexagonal PC do not invert because it is not periodic along the x -direction. For ω_n near zero, $\lambda_0 \gg a$, so the lattice behaves like a homogeneous medium, and the corresponding IFCs are circular [42]. At larger ω_n , where $\lambda_0 \sim a$, the lattice exhibits strong spatial dispersion that manifests as SC. Comparing across bands at fixed ω_n , the lowest-order bands have the flattest IFCs, indicating stronger SC in the lower-order bands.

The strength of SC at a given ω_n can be quantified by the maximum deviation angle [58], defined as the maximum angle between the x -direction and the surface normal of the IFC of the first Brillouin zone. The maximum deviation angle across the first seven bands was calculated for a series of PCs having $r/a = 0.30 - 0.45$. The results (Figure 3.1c) show the maximum deviation angle is less than 6° for $\omega_n = 2.8 - 4.0$ and $r/a = 0.30 - 0.44$. It can be concluded that a hexagonal lattice of air holes offers broadband SC that is highly tolerant to variation in structural dimensions.

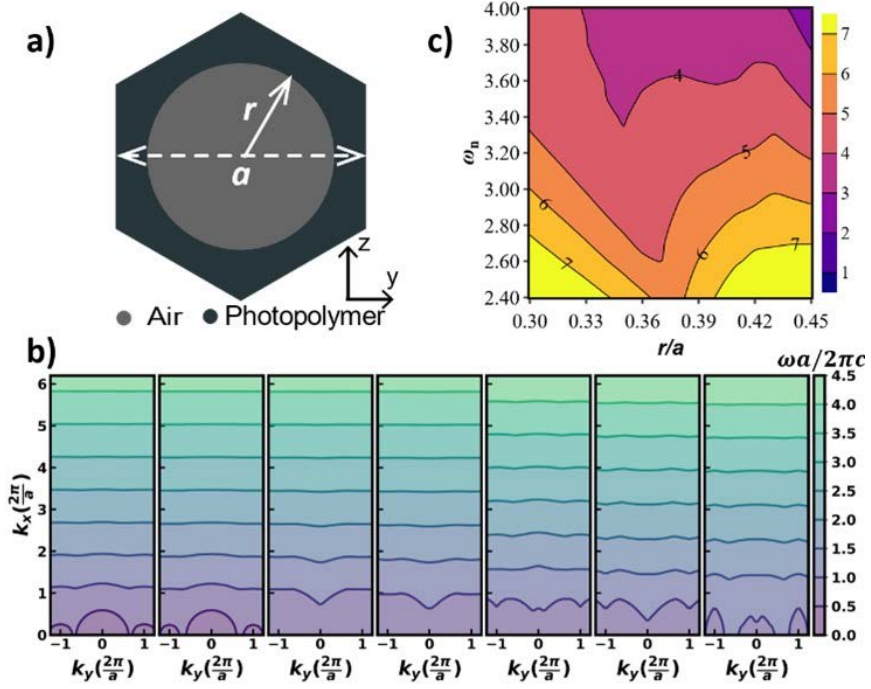


Figure 3.1: (a) Unit cell of hexagonal PC consisting of cylindrical air-holes in a photopolymer background. (b) IFCs of the first seven bands with $k_z = 0$ and wave vectors normalized to $2\pi c/a$. (c) Strength of SC for a range of PCs, shown as a contour plot of maximum deviation angle (in degrees) versus r/a and ω_n . Reprinted with permission from [59] © The Optical Society.

3.3. Fabrication and Structural Characterization

Hexagonal PCs were fabricated in the photopolymer "IP-Dip" (Nanoscribe) using an MPL system described elsewhere [46]. Around $\lambda_0 = 1.55 \mu\text{m}$, IP-Dip has negligible optical absorption, and its refractive index varies from $n = 1.515$ (low cross-linking) to $n = 1.525$ (high cross-linking) [57]. Varying n over this range did not significantly change the band calculations described above.

To operate at $\omega_n = 3$ and $\lambda_0 = 1.55 \text{ } \mu\text{m}$, the PC requires $a = \omega_n \lambda_0 = 4.65 \text{ } \mu\text{m}$. The PCs were fabricated with features 8% larger than targeted to offset shrinkage that occurs during post-exposure developing. Polymerized features were written mono-directionally at $50 \text{ } \mu\text{m s}^{-1}$ using average focused laser power $\langle P \rangle$ that was varied to achieve targeted feature sizes. A $3 \text{ } \mu\text{m}$ thick frame was fabricated around the lattice at high power ($\langle P \rangle = 3.5 \text{ mW}$, 10.7 GW/m^2) to support the PC and counter the effects of distortion and sagging. The lattice is supported by an array of short pillars, which enable it to shrink isotropically during developing, and fabricated atop a tower to raise it $120 \text{ } \mu\text{m}$ off the substrate. After exposure, structures were developed by immersing sequentially in propylene glycol methyl ether acetate (30 min., $\times 3$), isopropyl alcohol (5 min.), and deionized water (5 min.), then drained and allowed to dry in air.

The devices were structurally characterized by scanning electron microscopy (SEM). Images of a typical PC are shown in Figure 3.2. The hexagonal lattice is clearly visible as seven rows of air holes. No residual photopolymer is visible within air holes indicating the structure is well developed. The PC was fabricated for targeted dimensions of $a = 4.65 \text{ } \mu\text{m}$, $r/a = 0.35$, and a total extrusion length of $150 \text{ } \mu\text{m}$. Measurements yielded $\langle a \rangle = 4.75 \text{ } \mu\text{m}$ and $\langle r \rangle = 1.73 \text{ } \mu\text{m}$, with a relative standard deviation of 0.96% and 1.30%, respectively. The corresponding ratio $\langle r \rangle / \langle a \rangle = 0.363$. This and other structures could be reproducibly fabricated within 3% of the targeted dimensions.

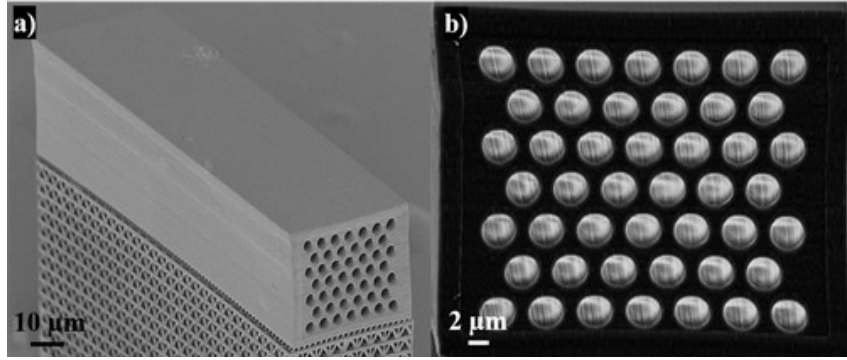


Figure 3.2: SEM images of a hexagonal PC with seven rows and seven columns of air holes and an extrusion length of 150 μm with targeted $r/a = 0.35$ and $a = 4.65 \mu\text{m}$. a) Side view and b) front views of the PC. Reprinted with permission from [59] © The Optical Society.

3.4. Optical Characterization and Results

Prior to SEM imaging, structures were optically characterized using a scanned-fiber system (Figure 3.3a). The light source consists of a femtosecond laser amplifier (Coherent Legend) pumping two optical parametric generators (OPGs). The signal beam (pulse duration ~ 120 fs, bandwidth ~ 30 nm) was used to characterize the PCs at $\lambda_0 = 1360$ nm - 1610 nm. Laser pulses were directed through a 10/90 cube beam splitter. The weaker beam was directed onto reference detector DET1 (Thorlabs PDA20H). The stronger beam passed through a polarizer and half-wave plate combination for polarization control and was then coupled into a source fiber (SF) using an objective lens. The opposite end of SF was positioned at the entrance face of the PC. Light exiting SF propagated through the PC and was collected with detection fiber DF connected to signal detector DET2 (Thorlabs PDA20H).

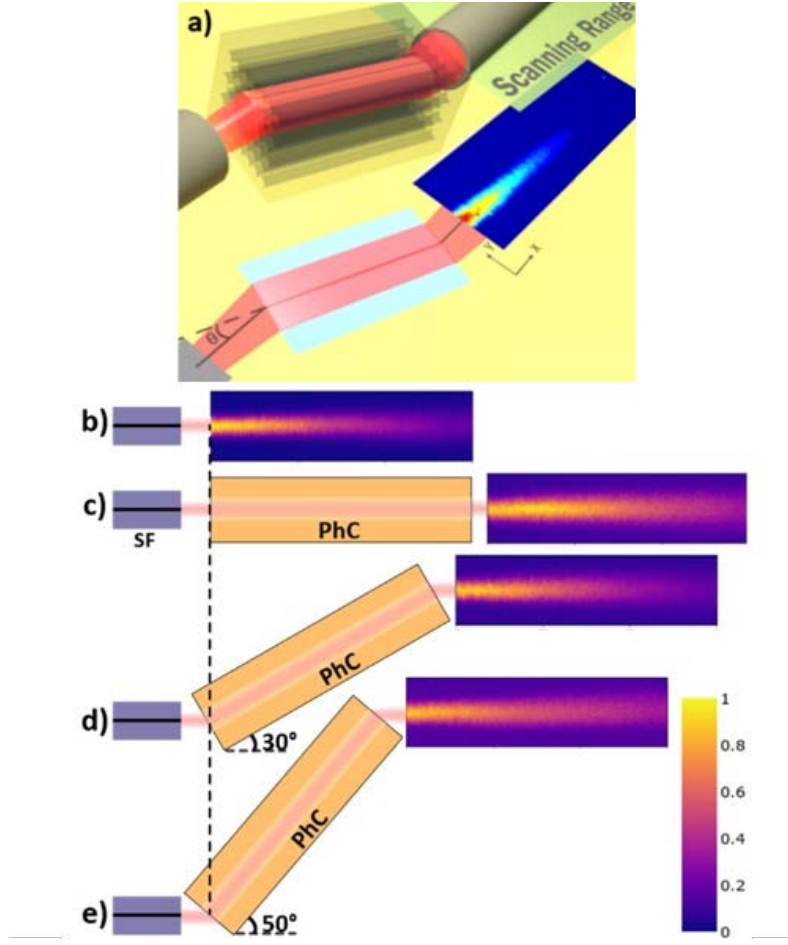


Figure 3.3: a) Schematic of the scanned-fiber system used to optically characterize the PCs. (c-e) Normalized intensity obtained by fiber-scanning at $\lambda_0 = 1550$ nm with b) no PC present and with the PC in the beam path oriented at angles c) $\theta_{\text{PC-fiber}} = 0^\circ$, d) $\theta_{\text{PC-fiber}} = 30^\circ$, and e) $\theta_{\text{PC-fiber}} = 50^\circ$.

Reprinted with permission from [59] © The Optical Society.

To prevent SF and DF (Thorlabs 1550 BHP, single mode, $NA = 0.13$) from dragging on the substrate, the ends near the PC were reduced in diameter to $30\ \mu\text{m}$ using buffered-oxide etch (J.T. Baker 1178-03). The tips of SF and DF near the PC were mounted on separate rotation- and

xyz-translation stages so that the light intensity could be measured as a function of angle and position. Data acquisition was automated using LabView. To reduce shot-to-shot noise, the signal from DET2 (I_{sig}) was referenced to that from DET1 (I_{ref}). Optical characterization was performed using a range of incident powers. The peak-irradiance reached 16 MW/m^2 without damaging the devices and was limited only by the available laser power and throughput of the characterization system.

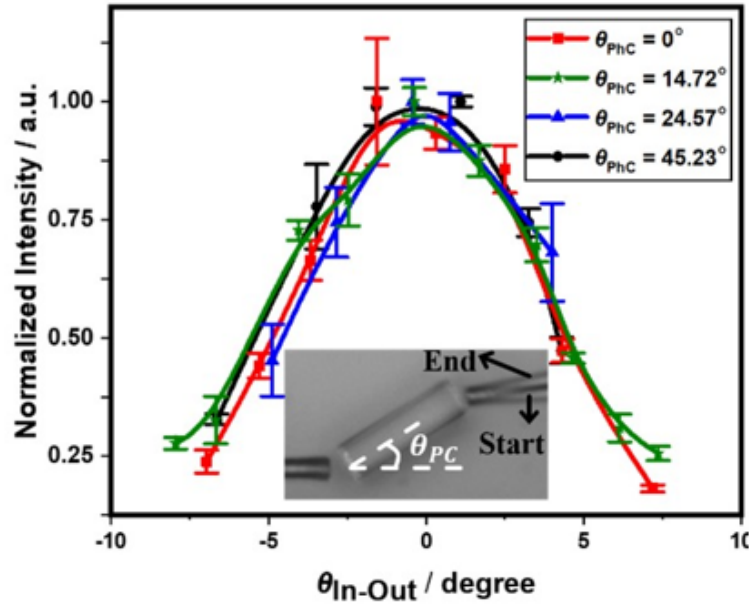


Figure 3.4: Angular intensity distribution of light with PC positioned at different angles. The inset is an optical image of the PC positioned between SF and DF. Reprinted with permission from [59] © The Optical Society.

Figure 3.3(b-e) show data acquired with the scanned-fiber system, where SF and DF are parallel. The incident light was polarized along the z -direction ($> 90\%$). DF was scanned

transversely (y-direction) from $-20\text{ }\mu\text{m}$ to $+20\text{ }\mu\text{m}$ ($0.5\text{ }\mu\text{m}$ step) and along the optic axis (x-direction) from $0\text{ }\mu\text{m}$ to $150\text{ }\mu\text{m}$ ($1\text{ }\mu\text{m}$ step). Light exiting SF gently diverges as expected (Figure 3.3b). Figure 3.3(c-e) show intensity plots with the PC inserted between SF and DF and oriented at angles of 0° , 30° , and 50° with respect to the optic axis. After traversing a full $150\text{ }\mu\text{m}$ within the PC, light exits as a narrow, gently diverging beam, just as it does upon exiting SF. The intensity maps show that light propagates within the PC without diffracting. When the PC is rotated up to 50° , the beam still emerges from the center of the device. Also, the output beam tracks with the input beam when it is shifted laterally from the center of the PC (up to $\pm 8\text{ }\mu\text{m}$). Collectively, this behavior is consistent with light propagating due to SC [37].

Light exiting the PC was studied as a function of the angle of DF θ_{Out} and orientation of the PC θ_{PC} to develop better understanding of how energy propagates within the lattice. Because DF has a maximum acceptance angle of 7° , it only samples light traveling roughly parallel to its optical axis. Monitoring the intensity of light as DF is swept through θ_{Out} reveals the direction light travels upon exiting the PC. To prevent the PC from colliding with DF as angles are varied, DF was withdrawn by $10\text{ }\mu\text{m}$ from the exit face of the PC. Intensity at this position was then measured versus θ_{Out} . This type of scan was also carried out at $\theta_{\text{PC}} = 0^\circ$, 14.7° , 24.6° , and 45.2° , to obtain the data shown in Figure 3.4. All angles are referenced to a laboratory frame parallel to SF. Inspection of Figure 3.3(b) shows that light exits SF at $\theta_{\text{In}} = -2.5^\circ$ due to slight angling of the end face after cleaving. To correct for this deviation, the intensity in Figure 3.4 is plotted as $\theta_{\text{In-Out}} = \theta_{\text{Out}} - \theta_{\text{In}}$. In all cases, the intensity is maximum at $\theta_{\text{In-Out}} = 0^\circ$. Even when light couples into the device at oblique angle $\theta_{\text{PC}} > 0^\circ$, the original phase front is apparently maintained, so light exits the PC traversing along its original direction. In contrast, light transmitted through a monolithic

block with equivalent pathlength and $n_{\text{effective}} = 1.29$ (calculated using Maxwell-Garnett theory [60]) would walk off from center by $110\ \mu\text{m}$. This rules out interaction of light with the side-walls and propagation by total internal reflection because it would then exit parallel to the device, regardless of input angle, and the output would also be highly multi-mode.

If the PC self-collimates, light should propagate without diffraction, and the beamwidth before and after the PC should be the same. Intensity maps like those in Figure 3.3 were analyzed to extract the beamwidth as a function of distance from SF with and without the PC between SF and DF. The single-mode DF collects light across the width of its core, so the signal profile is a convolution of the mode profile with the intensity profile. To obtain actual beamwidths at a given distance from SF, the signal profiles were deconvoluted using the beamwidth obtained when SF and DF are coupled end-to-end. Measurements like those described above were repeated for several values of θ_{PC} and λ_0 .

Measurements of beamwidth obtained for a PC having $r/a = 0.35$ are shown in Figure 3.5, as the full-width at half-maximum (FWHM). The "ripple" present in the data is due to shot-to-shot variation in the laser output. When the beam exits SF and propagates in free space for $150\ \mu\text{m}$ (red trace), the beamwidth increases from $7\ \mu\text{m}$ to $15\ \mu\text{m}$ ($\pm 1\ \mu\text{m}$) due to natural divergence. In contrast, when the beam travels an equivalent distance within the PC (yellow, green, and blue traces), it emerges unbroadened. These data show that SC within the lattice suppresses natural beam spreading due to diffraction. Similar results are obtained when the orientation of the PC is varied by $\theta_{\text{PC}} = 0^\circ - 50^\circ$ and when the wavelength is $\lambda_0 = 1360\ \text{nm}$, $1550\ \text{nm}$, and $1610\ \text{nm}$. SC in the hexagonal PC is tolerant to large variation in the input-coupling angle, and the response is

broadband, spanning the *E*- and *L*-bands used in telecommunications. For all input angles, the beam exiting the lattice diverges faster than the input beam. This could be due to multi-mode excitation within the lattice or imperfect SC.

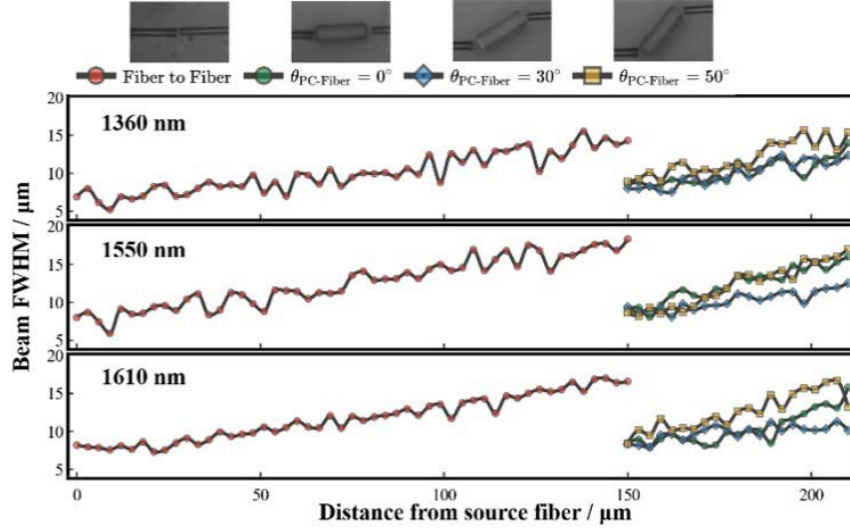


Figure 3.5: Beam divergence versus propagation distance with and without a PC between SF and DF. The top-, middle-, and bottom panels show data obtained for $\lambda_0 = 1360$ nm, 1550 nm, and 1610 nm, respectively. The red trace shows how the beam diverges when freely propagating in air over 150 μm . The green, blue, and yellow traces show how the beam diverges after exiting the PC when $\theta_{\text{PC}} = 0^\circ$, 30° , and 50° , respectively. Reprinted with permission from [59] © The Optical Society.

The power-throughput of the device η was estimated by integrating line scans measured with and without a PC present and calculating their ratio. When light is incident normal to the front face of the PC at $\lambda_0 = 1550$ nm, the power-throughput is high, reaching $\eta = 70\%$. When light is obliquely incident at a large angle of $\theta_{\text{PC}} = 50^\circ$, the power-throughput drops to $\eta = 49\%$. Similar

results were obtained for TM- and TE-polarized light, and also with a PC having $r/a = 0.40$ (not shown). Although the device maintains SC even when tilted to the input beam, power-throughput drops, most likely due to reduced input coupling at the entrance- and output faces. Distortions in the lattice can also introduce loss through scattering. Distortion is most evident for air holes near the edge of the lattice, but these minimally impact a beam travelling through the center of the lattice, where air holes vary in radius by only 1%. Such variation could be significant for longer interaction lengths in high-index lattices [40], but the effect is smaller for PCs comprised of low-index media. It should be possible to increase power-throughput by introducing structures on the input- and output faces that match external fields to modes within the PC.

3.5. Summary

The results reported here demonstrate the possibility of molding the flow of light using SC achieved in a 3D volumetric hexagonal PC fabricated with a low-refractive-index photopolymer. Light can be coupled into the hexagonal PC with an input acceptance angle of at least 50° ($NA = 0.76$). This figure compares well with previous work on 2D devices, which includes simulations showing all-angle SC ($NA = 1$) [61] and experimental work demonstrating acceptance angle up to 60° ($NA = 0.86$) [37]. The values reported here also compare favorably with flat interfaced waveguides and PC fibers, which offer input- NA in the range 0 to 0.5, as discussed in [62].

There are several noteworthy advances associated with the present work. The hexagonal PC does not require precise alignment for input-coupling, as light does not need to be pre-focused to a central guiding region. The hexagonal PC supports SC in a low-index lattice, which is more

easily fabricated than high-index lattices. It can be 3D printed by MPL, and it is a volumetric device that support truly-3D self-collimation. The hexagonal PC is continuous along the path that light travels, so its spatial mode properties are expected to differ significantly from those of conventional lattices which are periodic along the direction of propagation, and this topic is currently under investigation. The hexagonal PC should also support spatial variation, which enables independent control over phase [34] and direction of power flow [51]. This provides an additional route to compact photonic devices that perform more than one optical function. The hexagonal PC adds another class of structures with which integrated photonic systems can be developed to mold and control the flow of light.

4. CYLINDRICAL-LENS-EMBEDDED PHOTONIC CRYSTAL BASED ON SELF-COLLIMATION

Authored by Chun Xia, Jesus Gutierrez, Stephen Kuebler, Raymond Rumpf, and Jimmy Touma, the content of this chapter has been published in Optics Express on March 4th, 2022.

4.1. Introduction

The unit cells comprising a PC can be spatially varied throughout the lattice to further control how light flows within the device. Structural parameters that can be varied include the lattice spacing, material composition, unit-cell orientation, and unit-cell shape and anisotropy. The fill-factor can also be spatially varied to create graded refractive index (GRIN) devices. A wide range of GRIN-PCs having a complete bandgap have been reported, including a beam-bender [63], a lens [64], and a concentrator [65].

To date, GRIN-PCs based on *in-band* properties have been designed to operate at low frequency where IFCs are circular and $\lambda_0 \gg a$. The fill-factors of the unit cells are modulated to control the local refractive index, which can be estimated using the effective medium theory [66, 67]. Requiring IFCs to be circular limits the types and symmetries of lattices, and it makes it challenging to fabricate devices because the lattice period must be small compared to the wavelength. Consequently, GRIN-PCs operating at microwave and infrared wavelengths have been reported [65, 68-70], but devices operating at optical wavelengths are lacking.

Designing a GRIN-PC to operate using SC relaxes the restriction $\lambda_0 \gg a$. This makes it more practical to fabricate devices that operate at optical frequencies and over a wider range of

polarization states [61]. PCs having $a \sim \lambda_0$ can be fabricated by multiphoton lithography (MPL) [71] and nano-imprint lithography [72].

Rumpf et al. [73] reported an algorithm that can be used to design spatially-variant photonic crystals (SVPCs) in which one or more parameters of the lattice are varied globally while maintaining the shape of the unit cells locally so that SC is preserved throughout the device. The orientation of unit cells within a self-collimating lattice can be spatially-varied to create devices that direct the flow of optical power through a tight turn [51]. Simulations suggest that other structural features can be varied to control phase, polarization, or wavelength, in addition to power flow. Spatially varying two or more structural parameters opens a route to multi-functional devices that control power-flow, polarization, phase, or other characteristics of the light, all in a single device [34]. But this had yet to be demonstrated experimentally, until now.

The present work reports a new class of multi-function SVPCs, illustrated in Figure 4.1, that alter the phase of an optical field while independently controlling power flow. The example reported here is a lens-embedded SVPC (LE-SVPC). The LE-SVPC performs two fundamental functions in a single 3D nanophotonic device: (1) it directs the flow of optical power through SC, and thereby suppresses beam divergence; and (2) it reshapes the phase front along one axis, so the light cylindrically focuses *after* exiting the device. The LE-SVPCs are fabricated by MPL using the cross-linkable photopolymer IP-Dip (Nanoscribe), structurally characterized by scanning electron microscopy (SEM), and optically characterized at $\lambda_0 = 1550$ nm. Interestingly, although the LE-SVPC has a thickness several times the wavelength λ_0 , SC prevents focusing from

occurring within the device, so the optical behavior can be modeled as focusing by a perfectly thin cylindrical lens.

4.2. Design of the lens-embedded spatially-variant photonic crystal

4.2.1. Design concept

The LE-SVPC is based on the cubic unit cell shown in Figure 4.1a. The unit cell consists of a vertical wall of thickness t intersected by a transverse rod having an elliptical cross-section, with r_1 and r_2 giving the radii of the minor- and major-axes, respectively. The LE-SVPC is designed so light enters at a face parallel to the yz -plane and propagates along \hat{x} (optical axis). The unit cell is engineered to exhibit strong SC that forces light to propagate along one of the principal axes of the unit cell. Unit cells having period a repeat along \hat{x} , \hat{y} , and \hat{z} forming an LE-SVPC of lengths L_x , L_y , and L_z . Across the beam (parallel to \hat{y}), t varies from thick in the center to thin at the sides, creating an effective refractive index profile $n_{\text{eff}}(y)$ that impresses a quadratic phase profile onto the beam. SC prevents focusing from occurring within the lattice, so as power flows forward the wave accumulates a total phase delay determined by $n_{\text{eff}}L_x$.

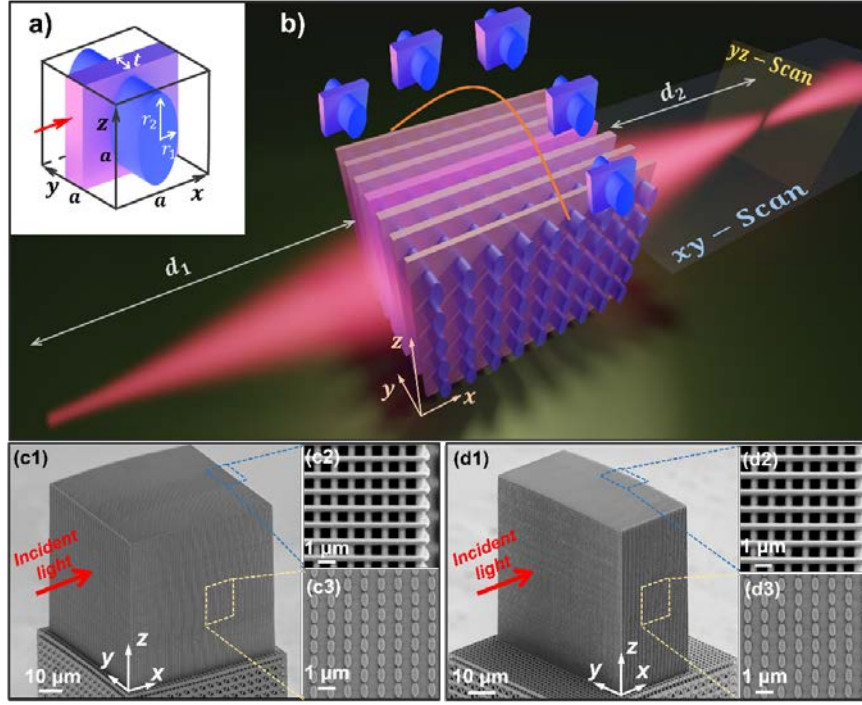


Figure 4.1: (a) Cubic unit cell upon which the LE-SVPC is based. The red arrow indicates the direction light is incident. (b) Diagram illustrating the behavior of a LE-SVPC. The lattice is comprised of unit cells whose wall thicknesses are varied parabolically from the center to the side. (c1, d1) SEM images of two LE-SVPCs fabricated by multi-photon lithography (MPL). Each has a transverse-area of 71×71 unit cells, but they differ in length. The long LE-SVPC (left) has a length along \hat{x} of $L_x = 71$ unit cells. The short LE-SVPC (right) has $L_x = 35$ unit cells. Panels c2 - c3 and d2 - d3 show zoomed-in views of the two LE-SVPCs from the top and side with the sample tilted by 65° . Reprinted with permission from [16] © The Optical Society.

4.2.2. Structure of the unit cell

The unit cell in Figure 4.1a is inspired by a study reported by Hamam et al. [56]. They found that a 2D lattice of alternating rods and walls offers broadband SC across a wide range of input angles. That particular unit cell is not suitable for the LE-SVPC because it is not 3D, and the rods and walls are disconnected, so it cannot form a free-standing, self-supporting structure. To arrive at the unit cell shown in Figure 4.1a, the 2D design of Haman et al. is modified as follows. The walls are extruded vertically (along \hat{z}). The rods, on the other hand, are elongated horizontally (along \hat{y}), so they penetrate the walls and connect to one another forming a connected lattice. Layers of horizontally oriented rods are then repeated vertically, separated by unit cell spacing a , to introduce periodicity and resulting SC that prevents the beam from spreading in the vertical direction as it propagates down the optical axis. The rods have an elliptical cross-section that can be adjusted to tune SC.

4.2.3. Optimizing self-collimation

The geometric parameters of the unit cell shown in Figure 4.1a were varied to find those which optimize SC. The ratio $t/a = 0.24$ was fixed while r_1/a and r_2/a were individually swept from 0 to 0.5, and the band diagram for each given unit cell was obtained using the plane wave expansion method (PWEM) [57]. In the calculations, the refractive index of the material was set to $n = 1.525$, for cross-linked IP-Dip at $\lambda_0 = 1550$ nm [49]. The quality of SC was judged using a figure of merit (FOM) described in [58]. The FOM consists of three performance metrics: the

frequency-bandwidth, angle of acceptance θ_c , and location of the inflection point of SC. The best SC was achieved when $r_1/a = 0.209$ and $r_2/a = 0.416$.

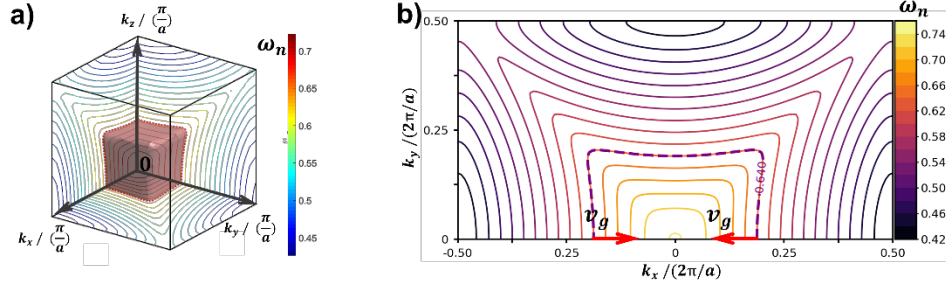


Figure 4.2: (a) A quadrant of the second TM band shown as one IFS at $\omega_n = 0.64$ and in-plane IFCs. (b) IFCs of the second TM band having $k_z = 0$. The IFC for $\omega_n = 0.64$ is indicated with the purple dashed line. Reprinted with permission from [16] © The Optical Society.

The frequency of operation is chosen where the IFC is flattest. IFCs for the second TM band (E -field polarized along \hat{z}) of the optimized unit cell are shown in Figure 4.2. Figure 4.2a shows only the first quadrant because the unit cell is symmetric about reflection through the xy -, xz -, and yz -planes. One complete IFS is drawn at $\omega_n = 0.64$. For other frequencies, only in-plane IFCs are shown. The IFS is flat where it is crossed by \vec{k} parallel to \hat{x} , \hat{y} , or \hat{z} , which indicates that light having ω_n corresponding to those values of \vec{k} will SC and propagate along the principal axes. Light is chosen to be incident along \hat{x} (red arrow in b), where θ_c is the largest. In this work, light is only introduced within the xy -plane, so k_z vanishes, and the allowed modes can be estimated well by 2D IFCs. The first two quadrants of IFCs are shown in Figure 4.2b because potentially two modes can be excited. At high frequency, the IFCs are concave. As ω_n decreases, the IFCs

shrink towards the center, flatten at $\omega_n = 0.64$, and become convex at low frequency. The LE-SVPCs were designed to operate at the inflection point, where $\omega_n = 0.64$, as indicated by red and purple dashed lines in Figure 4.2a and 4.2b, respectively. The second TE band also exhibits SC at $\omega_n = 0.64$ with a shape like that of the TM band. It is worth noting that the 3D unit cell employed in [51] also provides SC, but only for the TM mode.

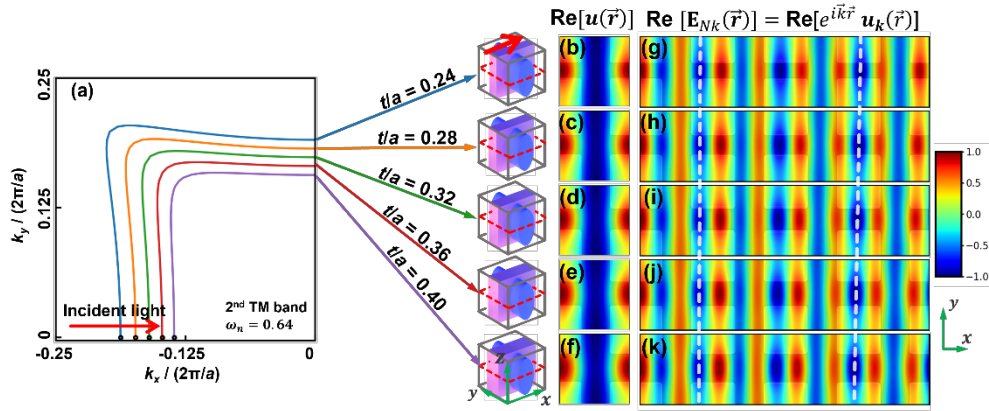


Figure 4.3: The shift of IFCs and change of mode profile for the second TM band at $\omega_n = 0.64$ as t/a varies from 0.24 to 0.40. (a) IFCs of the second TM band. Due to symmetry, only the second quadrant is drawn. The corresponding unit cells are shown at the right. The red dashed line indicates an xy -plane in which E_z is evaluated. (b-f) The real part of the eigenmodes calculated using PWEM. (g-k) Propagation of Bloch modes over four periods, calculated using FDTD. The light grey background shows the structure of the lattice within the xy -plane. Reprinted with permission from [16] © The Optical Society.

To embed a lens within the PC, a range of t was identified over which SC remains strong. Figure 4.3a shows how IFCs change for the second TM band at $\omega_n = 0.64$ when t/a increases from 0.24 to 0.40. The IFCs

move towards the origin, becoming flatter, and θ_c becomes wider. The corresponding electric field distributions and eigenmodes $\vec{u}(\vec{r})$ were obtained from PWEM. Figure 4.3(b) - 4.3(f) show the real part of $\vec{u}(\vec{r})$ within the xy -plane indicated by a red dashed line and superposed on a grey background that shows the profile of the underlying lattice. Along \hat{x} , $\vec{u}(\vec{r})$ peaks at the boundaries, is minimum in the center, and varies only slightly as the walls are thickened. Because the profile of $\vec{u}(\vec{r})$ is similar for all values of t , phase can vary smoothly between adjacent unit cells that have walls of slightly different thickness. Within $t/a = 0.24$ to 0.40 , wall thickness can be spatially varied to increase fill-fraction and introduce phase delay that reshapes the wavefront without losing SC.

Which mode is excited depends upon the properties of the incident light, such as frequency and direction of propagation, and the spatial dispersion of the lattice [74, 75]. The incident light only excites modes that have the same frequency. Maxwell's equations further require that the wavevector parallel to the boundary $k_{||}$ must be continuous. For example, consider a 2D unit cell having rotational symmetry for which the incident boundary is parallel to \hat{y} . Two mode-pairs can be identified, $(k_x, k_{||})$ and $(-k_x, k_{||})$, but only the one for which energy flows in the same direction as the incident beam can be excited. We apply these principles to a TM-polarized beam incident along the optical axis having $\omega_n = 0.64$. Only the modes having the same $k_{||}$ ($k_y = 0$) remain. If we look at IFCs of the second TM band at $\omega_n = 0.64$ shown in Figure 4.2b, we see that for the $(-k_x, 0)$ mode, ω_n increases as k_x increases. This implies dispersion is normal and power flows along the same direction as the incident light. On the other hand, for the $(+k_x, 0)$ mode, ω_n decreases as k_x increases, so dispersion is anomalous, and power would have to flow opposite

to the incident beam. As such, only modes having $k_x < 0$ can be excited. The modes which can be excited when t is varied are indicated in Figure 4.3a by the black dots placed along the k_x -axis.

4.2.4. Engineering optical phase delay

The finite-difference time-domain (FDTD) method and PWEM were used to calculate how light propagates within a uniform lattice based on the unit cell in Figure 4.1a, for a range of wall thicknesses t . These data were used to obtain a relationship between t and $n_{\text{eff}}(t)$ with which the LE-SVPC could be designed to generate a quadratic phase profile.

The wave vector \vec{k} and effective refractive index n_{eff} of a uniform lattice having a fixed value of t can be uniquely determined with FDTD. These simulations give phase information of an electromagnetic field propagating in a lattice. For a plane wave that takes the form of $\exp(i\vec{k} \cdot \vec{r})$, its wavefront is well defined, and its phase velocity is given by $\omega/|\vec{k}|$. Once \vec{k} is known, the refractive index n can be calculated with

$$n = \frac{|\vec{k}|}{k_0} \quad (4.1)$$

where $k_0 = 2\pi/\lambda_0$. However, waves propagating inside of PCs are Bloch modes and can be expressed as [25]

$$E_{Nk}(\vec{r}) = u_k(\vec{r}) \exp(i\vec{k} \cdot \vec{r}) \quad (4.2)$$

where N is band number and $u_k(\vec{r})$ is a complex amplitude function that has the same periodicity as the lattice. Phase velocity must be determined with care because the wavefront is not uniform due to modulation by $u_k(\vec{r})$. By looking at phase accumulated between a pair of points parallel to \hat{x} and separated by integer multiple of a , the contribution to phase from $u_k(\vec{r})$ vanishes leaving only the phase accumulated due to $\exp(i\vec{k} \cdot \vec{r})$. The residual phase can be used to calculate \vec{k} , which is substituted into Eq. 4.1 to find n_{eff} .

The FDTD simulations were performed using the open-source software MEEP [76]. The light source was a vertically polarized plane wave (electric field parallel to \hat{z}) launched parallel to \hat{x} with $\lambda_0 = 1550$ nm. The corresponding lattice constant $a = \omega_n \lambda_0 = 992$ nm. The grid was periodic along \hat{y} and \hat{z} to mimic an infinite lattice. Parallel to \hat{x} , the boundaries were set to perfectly matched layers (PMLs) to avoid non-physical reflections. Field propagation was calculated with lattices having the parameter t varied as shown in Figs. 4.3(b) - 4.3(f). Convergence was verified for grid resolution, PML thickness, and the total time steps. The converged results are shown in Figs 4.3 (g) - 4.3(k) as the real part of E_z , sampled within the plane identified in Figs. 4.3(b) - 4.3(f), and propagated along \hat{x} over four lattice periods. The dashed white lines identify positions of equal phase. Phase advances slower in a lattice with thick walls, indicating the effective refractive n_{eff} increases as t increases. With care for phase wrapping, n_{eff} was calculated by evaluating phase difference between a pair of points along \hat{x} and separated by an integer multiple of the lattice spacing a . It is worth noting that the n_{eff} obtained does not depend on the choice of point pairs with the yz -plane. Initially, n_{eff} increases and then stabilizes after roughly three unit cells as the input plane wave transforms to a Bloch mode. The stabilized n_{eff}

obtained for a range of t/a is plotted in Figure 4.4. As t/a increases from 0.24 to 0.40, n_{eff} increases linearly from 1.266 to 1.351. The values of n_{eff} lie between that of vacuum and the bulk polymer, and the maximum Δn_{eff} is 0.085.

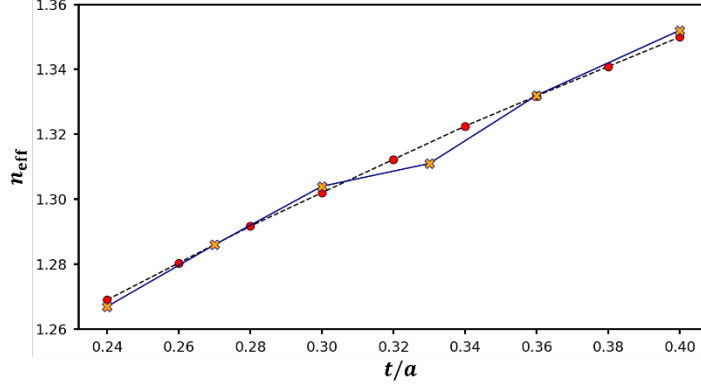


Figure 4.4: Relationship between t/a and n_{eff} extracted from FDTD (yellow cross) and PWEM (red dot) simulations for the TM mode. Reprinted with permission from [16] © The Optical Society.

PWEM can be used to confirm n_{eff} if information lost from band folding is recovered with help from the FDTD simulations. Band diagrams are typically shown for the first Brillouin zone (FBZ). For modes in the first band, \vec{k} can be read off directly. Folding must be considered for obtaining \vec{k} in higher-order bands. The unfolded \vec{k} can be determined by first shifting \vec{k} by integers of the width of the FBZ, calculating n_{eff} using Eq. 4.1, and identifying which value of n_{eff} agrees with that from FDTD simulations. It was found that \vec{k} read directly from Figure 4.3a must be shifted up by one FBZ-width to obtain the unfolded \vec{k} . Values of n_{eff} obtained from PWEM after unfolding are plotted in Figure 4.4 and found to agree to within 0.8% with those

obtained from FDTD calculations. The relationship in Figure 4.4 was used to determine how thick the walls of the unit cells must be to achieve n_{eff} at a given horizontal position y across the LE-SVPC.

The LE-SVPC is designed to have a phase distribution given by

$$\Delta\phi = \phi(y) - \phi(0) = -\frac{\pi}{\lambda_0 f} y^2 \quad (4.3)$$

where f is the focal length and $\Delta\phi$ is the phase difference at y relative to the center of the LE-SVPC at $y = 0$. Assuming light travels parallel to the optical axis due to SC, $\Delta\phi$ does not depend on $u(\vec{r})$ but is instead uniquely determined by $\exp(i\vec{k} \cdot \vec{r})$ and can be expressed as

$$\Delta\phi = \phi(y) - \phi(0) = k_0[n_{\text{eff}}(y) - n_{\text{eff}}(0)]L_x \quad (4.4)$$

Substituting Eq. 4.3 to Eq. 4.4 and solving for $n_{\text{eff}}(y)$ gives

$$n_{\text{eff}}(y) = n_{\text{eff}}(0) - \frac{y^2}{2fL_x} \quad (4.5)$$

Knowing how $n_{\text{eff}}(y)$ must change across the device, the relationship in Figure 4.4 can be used to obtain $t(y)$ that defines the physical profile of the LE-SVPC for a given f . Similarly, when $n_{\text{eff}}(y)$, $n_{\text{eff}}(0)$, and L_x are known, f can be calculated with Eq. 4.5 rearranged as

$$f = \frac{y^2}{2L_x[n_{\text{eff}}(0) - n_{\text{eff}}(y)]} \quad (4.6)$$

4.3. Fabrication and characterization

4.3.1. Fabrication method

The LE-SVPCs were configured to function at $\omega_n = 0.64$ and $\lambda_0 = 1550$ nm. The corresponding targeted dimensions are then $a = \omega_n \lambda_0 = 992$ nm, $r_1 = 208$ nm, $r_2 = 413$ nm, and t parabolically decreases in width from $t/a = 0.40$ at the center ($t_{\text{thick}} = 397$ nm) to $t/a = 0.24$ ($t_{\text{thin}} = 238$ nm) at the side.

LE-SVPCs were fabricated using a home-built MPL system. The laser source is a mode-locked Ti:sapphire laser (Coherent) producing 120 fs pulses at a repetition rate of 76 MHz and a center-wavelength of 800 nm. The linearly polarized beam is passed through an acousto-optic modulator (Gooch and Housego) to adjust the average exposure power $\langle P \rangle$ and then expanded by a telescope to overfill an objective lens (Nikon, 60 \times , $NA = 1.4$). The lens focuses light into the photopolymer to activate polymerization at the focal spot. A calibrated integrating sphere (Optronic Laboratory 731) is used to measure $\langle P \rangle$ after the lens. Borosilicate glass microscope slides were used as substrates for fabrication. An adhesion layer was added by spin-coating 1 vol-% (3-acryloxypropyl)trimethoxysilane (CAS# 4369-14-6) in methanol (CAS# 67-56-1) onto the substrate (2500 rpm, 30 s), baking on a hotplate (90 $^{\circ}\text{C}$, 30 s), then allowing it to cool in air. The substrate was mounted on a three-axis nanopositioner (Physik Instrumente 563.3CD), a drop of IP-Dip was added, and the objective was lowered into the photopolymer. The pattern of the LE-SVPC was exposed under control of a microcomputer that coordinates the movement of the stage (50 $\mu\text{m s}^{-1}$) with adjustment of $\langle P \rangle$. Following exposure, structures were developed by immersing sequentially in propylene glycol methyl ether acetate (PGMEA, 30 min, 3 \times), isopropyl alcohol (IPA, 5 min), and deionized water (5 min). Afterwards, the samples were drained and left to dry in the air.

The devices were fabricated along with a tower that elevates the structure off the supporting substrate to facilitate optical characterization. $\langle P \rangle$ was varied as needed to create walls having the targeted thickness. Rods with elliptical cross-section were created with three partially overlapping and adjacent exposure lines. The central line was exposed at high power ($\langle P \rangle = 1.87$ mW). The outer lines were exposed at low power ($\langle P \rangle = 1.48$ mW) and laterally offset from the center line by +97 nm and -97 nm, respectively. The fabrication time for the PCs shown in Figure 4.1(c1) and Figure 4.1(d1), excluding the supporting towers, was 27 hours and 20 hours, respectively.

4.3.2. Structural characterization

LE-SVPCs were structurally characterized using SEM images. Figure 4.1c(1) and 4.1d(1) show two typical devices. Each was fabricated to have the same t -profile and transverse dimensions $L_y = L_z = 71$ unit cells, but their lengths differ. A short device having $L_x = 35$ unit cells and a long device having $L_x = 71$ unit cells were created to study how length effects focal power.

Measurements of the periodicity and the dimensions of walls and elliptical rods were obtained from the SEM images. The periodicities of the LE-SVPC shown in Figure 4.1c(1) are 1010 nm, 945 nm, and 987 nm along \hat{x} , \hat{y} , and \hat{z} , which differ from the targeted periodicity by 1.7%, 4.8%, and 0.5%, respectively. For the rod geometry, r_1 and r_2 are 201 nm and 414 nm, which differs from the targeted dimensions by 3.3% and 0.1%, respectively. The LE-SVPCs shown in Figure 4.1c(1) and Figure 4.1d(1) were fabricated back to back and their measured structural parameters are similar.

To verify that t follows the targeted quadratic profile, wall thicknesses of the LE-SVPC shown in Figure 4.1c(1) were measured on the input face, where walls intersect rods. The values obtained are shown in Figure 4.5 and are fitted to a second-order polynomial. The variation in wall thickness is visibly parabolic, differing from the fitted curve by no more than 4%. The t -profile of the LE-SVPC in Figure 4.1d(1) varies similarly (*not shown*) but has an overall offset of 17 nm, which cannot adversely affect the wavefront because n_{eff} varies linearly with t .

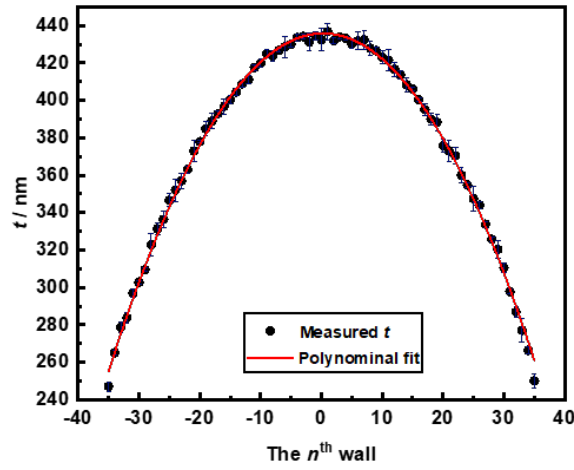


Figure 4.5: Profile of wall-thickness t across the LE-SVPC (parallel to \hat{y}) shown in Figure 4.1c(1). Measured values of t are plotted as black dots. The solid red line shows a fit of the measurements to a second-order polynomial. The error bars represent the ± 1 standard deviation of five measurements. Reprinted with permission from [16] © The Optical Society.

The PWEM calculations were repeated using the experimentally measured dimensions to determine how deviation from the targeted form affects the optical properties of the LE-SVPC. The maximum Δn_{eff} was found to be 0.0965 and 0.0777 for vertically and horizontally polarized

light, respectively, which compares well with the targeted Δn_{eff} . The PWEM simulations also show that deviations from the targeted design do not significantly alter the shape of the IFCs nor the resulting strength of SC. The values of Δn_{eff} obtained for the fabricated LE-SVPC in Figure 4.1c(1) were substituted into Eq. 4.6 to obtain the theoretical focal length as $f = 81 \mu\text{m}$ and $99 \mu\text{m}$ for vertically and horizontally polarized light, respectively.

4.3.3. Method of optical characterization

LE-SVPCs were optically characterized at the wavelength $\lambda_0 = 1550 \text{ nm}$ using a scanned-optical-fiber system (Figure 4.1), the details of which are reported elsewhere [59]. In brief, single-mode optical fibers (ThorLabs 1550 BHP) were used to couple laser light into the device and observe how light propagated upon exiting. Light from the source fiber (SF) propagated distance d_1 along \hat{x} as a gently diverging Gaussian beam [77] before illuminating the entrance face of the LE-SVPC. Light exiting the device traveled distance x before being sampled by a detection fiber (DF) coupled to a photodiode. The output was referenced to the reading from an external detector to eliminate fluctuations due to shot-to-shot variation of the laser-pulse energy. The referenced signal $S(x, y, z)$ was recorded as the DF scanned through the beam to obtain spatial intensity maps. The coordinate system is shown in Figure 4.1, and position $x = 0$ is located at the exit-face of the LE-SVPC. The positions of the SF, LE-SVPC, and DF were observed from above with an optical microscope and corresponding images were used to confirm values of d_1 and x .

Scans of S within a yz -plane were used to observe the transverse profile of the beam at a given x along the propagation direction. Scans within an xy -plane were used to observe how the

transverse profile changed with x , and the horizontal width of $S(x)$ was taken as its full-width at half-maximum (FWHM). Scans were repeated multiple times, with SF shifted to different distances d_1 , to explore how curvature and size of the incident beam affected focusing by the LE-SVPC.

The referenced signal S is actually a convolution of the intensity of the propagating beam with the input-response function of DF, so the FWHM of $S(x)$ is not the true beam width. The FWHM converges to the beam width when it is large relative to the mode-field diameter of the DF, and both the beam width and the FWHM of $S(x)$ are minimum at the focal point. The FWHM of the beam itself can be extracted by deconvolution, and the spatial profile and FWHM of $S(x)$ can be modeled when the distribution of intensity and phase of the beam are specified.

4.3.4. Example of optical characterization

Figures 4.6a(1-4) and 4.6b(1-4) show results from the optical characterization of a long- and short LE-SVPC, like those in Figs. 4.1c(1) and 4.1d(1). The source light was vertically polarized. The scans were started at $x = 10 \mu\text{m}$ to avoid colliding the DF with the LE-SVPC. Figures 4.6(a3) and 4.6(b3) are examples of xy -scans, obtained with $d_1 = 150 \mu\text{m}$. Measures of FWHM obtained from xy -scans are plotted in Figs. 4.6(a4) and 4.6(b4). The data were fitted to a fourth-order polynomial, then the point where FWHM was minimized was identified, and the corresponding value $d_2 = x$ was recorded as the focal distance. When a fit yielded $R^2 < 0.9$, a higher-order polynomial was used. Values of d_2 obtained from fourth- and higher-order polynomials differed by less than $5 \mu\text{m}$. This value is comparable to the minimum step-size in x

used to record the scans and is therefore taken as a reasonable estimate for the uncertainty of d_2 . To measure the minimum beamwidth FWHM_{\min} more accurately, the DF was moved to the focal spot d_2 and line-scans parallel to \hat{y} were recorded three times. The final value of FWHM_{\min} was obtained as an average from three scans.

The plots of FWHM show that beams exiting the LE-SVPCs become narrower along \hat{y} , then reach a minimum width and begin to diverge. The green dashed lines indicate the point $d_2 = x$, where FWHM_{\min} is located and where the transverse profiles were recorded. For comparison, profiles obtained without the LE-SVPC are also shown. When the device is present, the profile narrows in the horizontal axis and becomes elliptical, which is consistent with the LE-SVPC functioning like a cylindrical lens. The long LE-SVPC produces the narrower profile and therefore focuses stronger. It is worth noting that the point of maximum intensity appears before FWHM_{\min} . If a beam is focused by a rotationally symmetric lens, then the FWHM_{\min} and point of maximum intensity should appear at the same d_2 . But because the LE-SVPC focuses only along \hat{y} , the beam exiting the LE-SVPCs converges along \hat{y} and diverge along \hat{z} , causing the point of maximum intensity to appear before FWHM_{\min} .

Measurements were performed on multiple, separately fabricated LE-SVPCs, like those in Figure 4.1. The uncertainties in FWHM_{\min} and the corresponding focal distance were estimated from the analysis of xy -scans obtained with three separate long- and short devices. The PCs were characterized with SF positioned at several distances d_1 . When $d_1 = 100 \mu\text{m}$, the FWHM_{\min} and d_2 differed between scans by less than $0.33 \mu\text{m}$ and $5 \mu\text{m}$, respectively, for both polarizations. When $d_1 = 150 \mu\text{m}$, FWHM_{\min} and d_2 differed by less than $0.16 \mu\text{m}$ and $6 \mu\text{m}$, respectively.

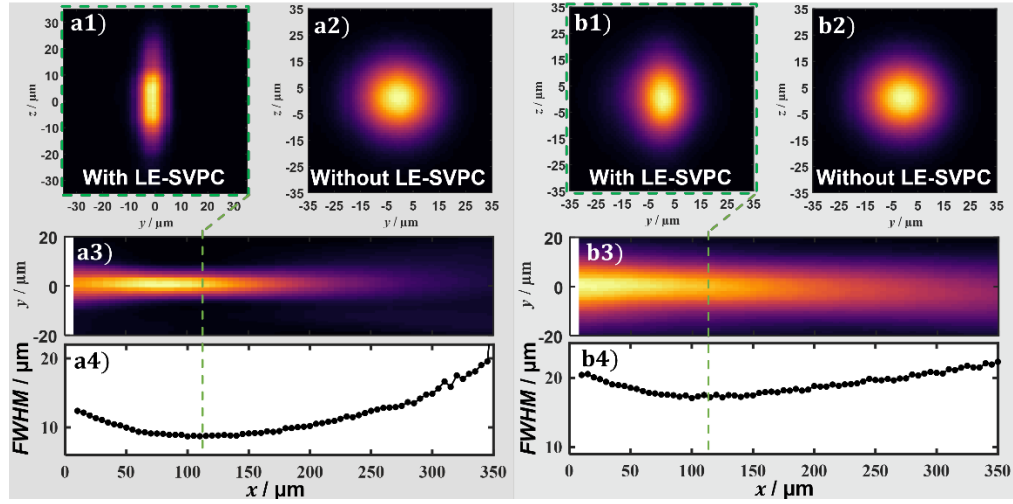


Figure 4.6: Optical characterization of two LE-SVPCs like those shown in Figs. 4.1c(1) and 4.1d(1), having (*left*) $L_x = 71$ unit cells and (*column*) $L_x = 35$ unit cells, and measured with $d_1 = 150 \mu\text{m}$. Panels (a3) and (b3) are xy -scans that show how the transverse beam profile changes along \hat{y} when light exits the LE-SVPC and propagates distance x . These data were used to obtain the width of the scan-profiles as FWHM versus x , shown in (a4) and (b4). Green dashed lines identify focal points $d_2 = x$, where the beam is narrowest along \hat{y} and where FWHM_{\min} is located.

At these points, full transverse scans of the beam profile appear as seen in (a1) and (b1). For comparison (a2) and (b2) show transverse profiles recorded without the LE-SVPC present. When the LE-SVPC is present, the beam narrows in the horizontal plane, showing the device behaves like a cylindrical lens, and the focal power is stronger for the longer LE-SVPC. Reprinted with

permission from [16] © The Optical Society.

4.4. Modeling as a thin lens

The performance of the LE-SVPC can be modeled as illustrated in Figure 4.7a. If the LE-SVPC behaves as designed, then SC should force light to propagate through the device without diverging or focusing, even as the beam accumulates phase across its transverse profile. Light exiting the SF propagates as a diverging, rotationally symmetric Gaussian beam [77], then couples into the LE-SVPC. Geometrically, rays should enter and exit the device at the same position, and light should focus only *after* exiting the device. It follows then that it should be possible to model the LE-SVPC as a *thin* lens, even though it is physically thick.

It is well known that a Gaussian beam incident on a thin lens focuses also to a Gaussian beam [78]. The waist of the source beam w_{01} at distance d_1 can be related to the waist of the focused beam w_{02} at distance d_2 through the focal length f using two principles. First, the source- and focused beams must have identical widths at the front and back surfaces of the lens. This equality expressed in Eq. 4.5 is obtained by propagating the source beam forward to the lens over d_1 and propagating the focused beam back to the lens over d_2 . The method used to propagate the Gaussian beam is described in [78].

$$(w_{01}^2 + \frac{d_1^2 \lambda_0^2}{\pi^2 w_{01}^2}) = (w_{02}^2 + \frac{d_2^2 \lambda_0^2}{\pi^2 w_{02}^2}). \quad (4.7)$$

Second, the forward- and back-propagated beams must have identical phase fronts at the exit-face of the lens. The phase of the forward-propagating beam is given by its radius of curvature at the entrance face $R_1(d_1)$ plus the additional phase acquired upon propagating through the lens. The phase of the backward-propagated beam is given by its radius of curvature at the exit-face $R_2(d_2)$. These quantities can be related by taking the derivative of the phase fronts, giving

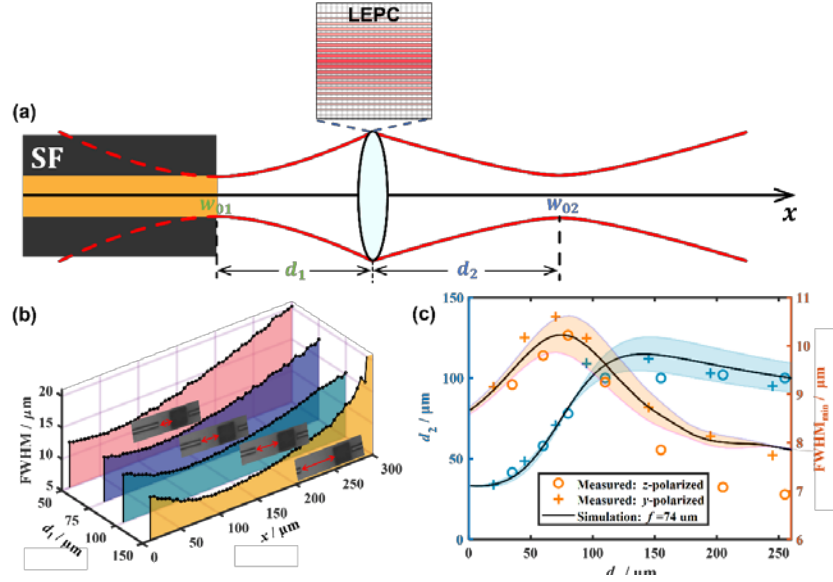


Figure 4.7: Optical modeling and characterization of focusing by LE-SVPCs. (a) Schematic of the model. Light emanates from a single-mode optical fiber (SF) as a Gaussian beam of width w_{01} , propagates distance d_1 , then couples into the LE-SVPC, which is treated as a thin lens. SC forces light to travel the length of the device without spreading or focusing, even as it accumulates a quadratic phase profile. Upon exiting, the light focuses to a Gaussian beam of width w_{02} after propagating distance d_2 . Because SC prevents the beam width from changing within the LE-SVPC, it can be treated as a thin lens. (b) Experimental measurements of FWHM as a function of distance x when $d_1 = 50 \mu\text{m}$, $75 \mu\text{m}$, $100 \mu\text{m}$, and $150 \mu\text{m}$, after passing through the long LE-SVPC, like that in Figure 4.1(c1). (c) Experimental and simulated change of d_2 and FWHM_{\min} for a long LE-SVPC as a function of d_1 , with vertically (\hat{z}) and horizontally (\hat{y}) polarized light. The shaded region shows how d_2 and FWHM_{\min} vary in simulation when f changes by $\pm 5 \mu\text{m}$. Reprinted with permission from [16] © The Optical Society.

$$\frac{1}{R_1(d_1)} + \frac{1}{R_2(d_2)} = \frac{1}{f}. \quad (4.8)$$

Equations (1) and (2) can be solved to find d_2 and w_{02} when d_1 , w_{01} , and f are known, or they can be used to find f when w_{01} , d_1 , w_{02} , and d_2 are known. In this work, solutions were found numerically using the *Equations and Systems Solver* in MATLAB (R2018a). The waist of the source beam w_{01} was measured experimentally with the process described in [59] and found to be $5.7 \mu\text{m}$.

To compare with experiment, values of w_{02} predicted from the thin lens model must be converted to FWHM of a line-scan. The energy collected by the DF is obtained by calculating the overlap integral between its response function and the complex field of the beam [79]. The response function is given by the complex field of the mode, which is described by zeroth-order Bessel functions of the first kind within the core and the second kind within the cladding region [80]. To emulate line-scans, the overlap integral is calculated progressively with the DF shifted virtually along y relative to the sampled beam, and the resulting scan-profile is used to calculate a simulated FWHM for comparison to the experiment.

4.5. Results and analysis

The width and curvature of a Gaussian beam affect where and how tightly it is focused by a given lens. To determine f of the LE-SVPC properly, FWHM and d_2 were measured with the source beam positioned at several distances d_1 from the device. Measurements like those shown in Figs. 4.6a(3) and 4.6a(4) were repeated for the long LE-SVPC at $d_1 = 50 \mu\text{m}$, $75 \mu\text{m}$, $100 \mu\text{m}$, $150 \mu\text{m}$, $200 \mu\text{m}$, $250 \mu\text{m}$, and $300 \mu\text{m}$, and with the electric field of the source beam vertically or

horizontally polarized. Figure 7c shows how d_2 and FWHM_{\min} change versus d_1 . The solid lines in Figure 4.7c are theoretical values of d_2 and FWHM_{\min} , calculated using the thin-lens model with $f = 74 \mu\text{m}$. The values of FWHM_{\min} were obtained by convoluting the beam's electric field with the response function of the DF using the integral-overlap method. The blue and orange shaded regions show how widely d_2 and the FWHM_{\min} vary when f is varied by $\pm 5 \mu\text{m}$. The experimentally measured d_2 and FWHM_{\min} follow the same trend as the simulated curves, up to $d_1 = 200 \mu\text{m}$. Disagreement at $d_1 \geq 200 \mu\text{m}$ is expected because the incident beam has spread to the point that it overfills the LE-SVPC, so the Gaussian-focusing model no longer applies. The analysis shows that the focusing behavior of the LE-SVPC is well described by the thin-lens model.

The focal length f was estimated by regression analysis of the experimental data against simulations using a least-squares method. Regressions were performed on d_2 and FWHM_{\min} separately for all $d_1 < 250 \mu\text{m}$, yielding two values of f that could be compared. For the long LE-SVPC, f was found to be $68 \mu\text{m}$ and $70 \mu\text{m}$ for vertically polarized light, and $72 \mu\text{m}$ and $78 \mu\text{m}$ for horizontally polarized light. Weighting the two methods equally, the values can be averaged giving $f = 69 \mu\text{m} \pm 2 \mu\text{m}$ and $f = 75 \mu\text{m} \pm 3 \mu\text{m}$ for vertically and horizontally polarized light, respectively. Applying the same method to the short LE-SVPC gives $f = 138.5 \mu\text{m} \pm 8.5 \mu\text{m}$ and $f = 144 \mu\text{m} \pm 8.5 \mu\text{m}$ for vertically and horizontally polarized light. The uncertainty in f is larger for the short LE-SVPC because it focuses more gently, resulting in lower intensity at the focus and a poorer signal-to-noise ratio. The data show that the focal length decreases by half when the length of the LE-SVPC is doubled, as expected. The experimentally determined f is smaller than that obtained from theory. Given that the PWEM calculations on *uniform* lattices were used to obtain

n_{eff} and f , the gradient of t in the actual LE-SVPC and its effect on local n_{eff} is not considered. The stronger focusing observed experimentally suggests that spatially varying the unit cells produces a larger change in Δn_{eff} .

The power throughput η can be obtained from the integrated power transmitted through the LE-SVPC divided by the total power incident on the device. Directly integrating beam-profiles like those in Figure 4.6 and using these to calculate η overestimates throughput because the DF collects less power when the LE-SVPC is not present, and the beam is diverging. Loss due to the angular sensitivity of the DF can be compensated by calculating the integrated signal scaled by the response function of the DF using the overlap-integral method. In this way, the scaled throughputs were found to be $\eta = 85\%$ and $\eta = 90\%$ for the long- and short LE-SVPC, respectively.

The focusing behavior of the LE-SVPC was maintained even as the angle of incidence was varied for the input beam; however, the throughput dropped as the angle of incidence became more oblique. For example, the throughput of the long LE-SVPC dropped by 10%, 15%, 45%, and 78%, when the input beam was incident at 5° , 10° , 15° , and 20° , for vertically polarized light at $d_1 = 150 \mu\text{m}$. Yet, xy -scans at these angles show no significant change in d_2 or FWHM_{min} .

The unit cell of the LE-SVPC is asymmetric relative to the input polarization, so we should expect a birefringence that changes how vertically and horizontally polarized light focus. Unlike a conventional lens, for which the focal power depends on n_{eff} , the focal power of an LE-SVPC is determined by Δn_{eff} . The PWEM calculations show that $\Delta n_{\text{eff,vert}} > \Delta n_{\text{eff,horz}}$, so vertically polarized light is expected to focus more strongly, which is indeed observed experimentally.

If the device were a uniform lattice, then the birefringence would cause it to behave like a waveplate. But the LE-SVPC does not behave simply as a waveplate because n_{eff} varies with y causing focusing. If $\Delta n_{\text{eff,vert}}$ equaled $\Delta n_{\text{eff,horz}}$, then both polarizations would focus to the same point, and their superposition could yield another polarization state. Such a device would behave like a lens and a waveplate combined, similar to the meta-lens reported in [81]. For the LE-SVPCs reported here, the two polarizations focus separately, so they do not mix. Clearly, spatially-varied birefringent PCs can have rich polarization dependence, which itself may be exploited for new kinds of photonic devices.

The experiments discussed here do not provide direct evidence that light is self-collimated as it travels through the LE-SVPCs. However, the fact that f is halved when L_x is doubled indicates that the beam width does not change within the device, which is consistent with SC. It is worth noting that if d_1 is held constant, the beamwidth should be the same regardless of the length of the LE-SVPC through which it travels. Yet, this is not directly reflected in the experimental scans because the response function of the DF decreases as the interrogated beam becomes more curved, which makes the FWHM at $x = 0$ artificially smaller. The wavefront of light exiting the long LE-SVPC is more strongly curved than that exiting the short LE-SVPC. Consequently, the FWHM measured at $x = 0$ is about 7 μm smaller for the long LE-SVPC. To verify the source of this difference, the thin-lens model and overlap-integral methods were used to calculate FWHM at $x = 0$, assuming the values of f found by experiment, and indeed the more tightly focused beam yields a FWHM that is smaller by 6.4 μm .

The chromatic aberration of an LE-SVPC depends on the frequency dispersion of n_{eff} . Calculations performed versus wavelength suggest f varies by 0.8% per 100 nm around $\lambda_0 = 1550$ nm. Tighter focusing could be realized by either increasing the range over which t varies or increasing the length L_x of the lens. A tighter-focusing lens could still be compact by wrapping the phase, creating a Fresnel lens within the PC. When the device operates at 1550 nm and has t/a in the range of 0.24 to 0.40, $\Delta n_{\text{eff}} = 0.08$, which requires $L_x = 20$ μm to accumulate 2π phase.

A wide range of optical behaviors can be accessed by engineering the spatial dispersion of a PC, and subtle changes in structure can result in remarkably different properties. For example, Trull et al. [82] reported the optical properties of a polymeric woodpile PC that also exhibits focusing under certain conditions. The device is a *uniform* PC, but the structure of the unit cell produces *concave* IFCs that introduce anomalous dispersion at the operating wavelength. Because the IFCs are not flat, the PC does not self-collimate light *internally*. But under the conditions tested, anomalous dispersion of the lattice offsets the divergence of the input beam producing an on-axis output that is collimated, along with a complex series of off-axis diffracted beams.

The work reported here is distinct from that of Trull et al. in several ways. First, the unit-cell of the LE-SVPC is engineered to produce true SC within the lattice, and the spatial dispersion is sufficiently strong that the fill-factor can be varied to modulate phase and cause focusing without losing SC. Second, focusing does not occur at the input of the lattice, due to anomalous dispersion. Instead, the spatially-varied profile of fill factor and the resulting modulation in n_{eff} alters the phase front of the beam causing it to focus *after* exiting the device. Third, the method used to create LE-SVPCs is versatile. Focusing can be achieved without trying to match anomalous

dispersion of a uniform lattice to the divergence of an input beam. With the LE-SVPCs, the targeted phase profile is achieved by simply tuning fill-factor, using a single unit cell design. Many other phase profiles could in principle be achieved, including those that generate diverging beams at the output, or other more complex mode-profiles. The versatility results from spatial variation of the lattice.

4.6. Summary

This work demonstrates a path toward a new class of integrated photonic device – the LE-SVPC. The device is based on a strongly self-collimating lattice that forces light to propagate along principles axes without diverging (or focusing). The thickness of walls comprising the lattice are spatially varied to alter local n_{eff} and effect a change in phase across the beam. Upon exiting the device, the curved phase front causes the beam to focus. Mapping and analysis of the beam profile shows that the LE-SVPC behaves like an infinitely thin cylindrical lens. Processes are described for engineering the form of the unit cell and the structure of the LE-SVPC. PWEM simulations were used to design the unit cell so that it is tolerant to spatial variation and retains SC even when walls are thickened to alter the fill factor and resulting n_{eff} . FDTD and PWEM simulations were used in combination to calculate how n_{eff} varies with feature size in the unit cell.

In a sense, the LE-SVPC "programs" the light wave to focus so that it converges only after exiting the self-collimating lattice. The device could be thought of as a graded-refractive-index (GRIN) lens embedded in a self-collimating lattice. However, its performance is distinct from and simpler than conventional GRIN lenses, such as Luneburg lenses [70], because focusing does not

occur within the LE-SVPC. The phase-profile is engineered, and it can be simple parabolic, as in the present example, or more complex, such as an aberration-correcting profile. The lensing function of the LE-SVPC could be used to improve fiber-to-chip and chip-to-chip level interconnects. LE-SVPCs could also be integrated onto the tip of an optical fiber or microfluid channels for sensing and imaging applications. The orientation of the unit cells could in principle be spatially varied so the device bends power through a turn while generating a focusing wavefront. Embedding spatially programmed phase-shifting in a SC lattice is a general approach that could be used to create other types of integrated photonic devices such as mode converters.

5. BINARY-LENS-EMBEDDED PHOTONIC CRYSTALS

Authored by Chun Xia, Edgar Bustamante, Stephen Kuebler, Noel Martinez, Raymond Rumpf, and Jimmy Touma, the content of this chapter has been accepted for publication in Optics Letters in May, 2nd, 2022, and is expected to be published on May 27th, 2022.

5.1. Introduction

The concept of using SC for independent power and phase control has been discussed in Chapters 4, in which the concept was demonstrated experimentally with the report of a functional gradient-refractive-index lens-embedded PC (GRIN-LEPC). A GRIN lens was incorporated by spatially varying the thickness of walls across the lattice to adjust the effective refractive index. The approach requires precise control of feature size, and the device ends up relatively thick because large optical path difference is needed to achieve strong focusing, absent of phase wrapping.

The present work reports two new types of LEPC – the binary LEPC (B-LEPC) and the Fresnel B-LEPC (F-B-LEPC) shown in Figure 5.1 and Figure 5.3. The LEPCs are binary in that only two distinct wall thicknesses t are used to define a parabolically shaped lensing region. Inside and outside the lens-region, t is made large or small, respectively, to define regions of high and low effective refractive index n_{eff} . The B-LEPC is easy to fabricate and inspect because the outline of the lensing region is clearly visible by microscopy. The F-B-LEPC includes a Fresnel-type lens in which the phase of the lensing region is wrapped, producing a more compact device. The LEPCs were fabricated by multi-photon lithography (MPL) in the photopolymer "IP-Dip" (Nanoscribe)

and structurally characterized by scanning electron microscopy (SEM). Optical characterization and electromagnetic simulations are presented to explain the design and optical performance of B-LEPCs.

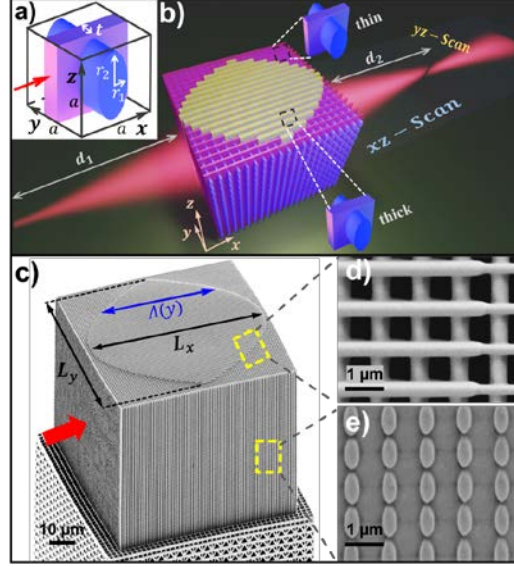


Figure 5.1: Binary-lens-embedded PC. (a) Unit cell. (b) Design of lattice. Inside (yellow) and outside (pink) the lens region, t is thick and thin, respectively. (c - e) SEM images of a B-LEPC having $71 \times 71 \times 71$ unit cells. (d) Top-view of walls transitioning from thick to thin. (e) Side-view of elliptical rods. Light is incident along the red arrow.

5.2. Design of the lens-embedded spatially-variant photonic crystal

The design of the B-LEPC is illustrated in Figure 5.1(b). Light is incident along \hat{x} . Across the beam (parallel to \hat{y}), a cylindrical lens is embedded by fabricating thick walls. The walls vary in length to introduce spatially varied optical path difference that curves the wavefront. SC forces

light to flow only along \hat{x} , neither spreading nor focusing, even as the beam accumulates phase through the lens. Curvature in the wave front causes the beam to focus only after exiting the lattice [13].

The B-LEPCs are comprised of the cubic rod-in-wall unit cell in Figure 5.1(a) having edge-length a . The rods have an elliptical cross-section with minor- and major-axes of radius r_1 and r_2 . Material comprising the lattice is treated as lossless with $n = 1.525$, as is known for cross-linked IP-Dip [14]. An optimization process described in [13] was used to calculate IFCs and analyze performance. The best SC is achieved with $r_1/a = 0.209$ and $r_2/a = 0.416$. SC appears at the second band for both TM and TE modes. The IFC are flattest at $\omega_n = 0.64$, and SC is maintained when t varies from $t_{\text{thin}} = 0.24a$ to $t_{\text{thick}} = 0.40a$. For $\lambda_0 = 1550$ nm, $a = \omega_n \lambda_0 = 992$ nm. The n_{eff} of a PC comprised of unit cells having thick or thin walls is denoted with n_{thick} or n_{thin} , respectively, and was calculated as in [13]. Briefly, the wavevector \vec{k} in the first Brillouin zone is found with the planewave-expansion method (PWEM) [15], and finite-difference time-domain (FDTD) simulations are used to correct \vec{k} for band-folding. Using the vacuum wave number k_0 gives $n_{\text{eff}} = |\vec{k}|/k_0$.

B-LEPCs were designed to reshape the wavefront as

$$\Delta\phi(y) = \phi(y) - \phi(0) = -\frac{\pi}{\lambda_0 f} y^2, \quad (5.1)$$

where $\Delta\phi(y)$ is the phase difference at y relative to the center of the lattice, and f is the focal length. The size of the lensing region along \hat{x} , \hat{y} , and \hat{z} is denoted by L_x , L_y , and L_z , respectively. Two extra unit cells were added around the lensing region to form the complete PC. Assuming light propagates parallel to \hat{x}

by SC, the total phase accumulated at y is $\phi(y) = |\vec{k}_0|[\Lambda(y)n_{\text{thick}} + \{L_x - \Lambda(y)\}n_{\text{thin}}]$, where $\Lambda(y)$ is the length of the thick walls, which span across multiple unit cells. With substitution, $\Delta\phi(y)$ becomes

$$\Delta\phi(y) = -|\vec{k}_0|\Delta n_{\text{eff}}[L_x - \Lambda(y)], \quad (5.2)$$

where $\Delta n_{\text{eff}} = n_{\text{thick}} - n_{\text{thin}}$. Combining Eqs. (1) and (2) and solving for $\Lambda(y)$ shows that thick walls must vary in length parabolically across the lensing region as:

$$\Lambda(y) = L_x \left(1 - \frac{4y^2}{L_y^2}\right), \quad (5.3)$$

and the focal length f is given by

$$f = \frac{L_y^2}{8\Delta n_{\text{eff}}L_x}. \quad (5.4)$$

A B-LEPC can be converted to a F-B-LEPC by embedding a wrapped-phase profile while retaining the aperture size and choice of t_{thick} and t_{thin} . Figure 5.3(a1) shows the Fresnel equivalent of the B-LEPC in Figure 5.1(c). Upon wrapping phase, the $\Lambda(y)$ profile of Eq. 5.3 becomes

$$\Lambda(y) = L_{\text{FB}} - \frac{\text{wrap}(\Delta\phi)}{k_0\Delta n_{\text{eff}}}, \quad (5.5)$$

where L_{FB} is the physical length of the Fresnel zone. L_{FB} can be chosen arbitrarily as long as $L_{\text{FB}} > L_{\text{min}}$, where L_{min} is the minimum needed to achieve $\Delta\phi = 2\pi$. Using Eq. 5.2 with $\Delta n_{\text{eff}} = 0.0725$ and $\lambda_0 = 1550$ nm gives $L_{\text{min}} = 21.4$ μm , or 22 unit cells. To strengthen the lattice, L_{FB} was set to 26 unit cells, and two additional unit cells having thin walls were added around the perimeter to give an overall length $L_0 = 30$ unit cells.

5.3. Fabrication and structural characterization

5.3.1. Binary-Lens-Embedded photonic crystals

B-LEPCs were created using an MPL system and processes described in [16]. The devices were fabricated atop a tower that elevates the structure off the supporting substrate to facilitate optical characterization. The targeted t_{thick} and t_{thin} are $0.24a$ and $0.36a$, respectively. Walls were patterned as continuous lines across the PC, and the average laser power $\langle P \rangle$ was changed as the focal spot moved outside (1.48 mW) or inside (2.15 mW) the lensing region. Rods with elliptical cross-sections were created by patterning three adjacent lines laterally offset in \hat{x} by ± 97 nm. The central line was exposed at $\langle P \rangle = 1.87$ mW, and the outer lines were exposed at $\langle P \rangle = 1.48$ mW.

The B-LEPC in Figure 5.1(c) is designed to have $L_x = L_y = L_z = 71a$. The average dimensions were measured from SEM images like those in Figure 5.1(d) and Figure 5.1(e) and found to match targeted dimensions within experimental error. The unit-cell spacings along \hat{x} , \hat{y} , and \hat{z} are 1010 nm (1.8%), 997 nm (0.5%), and 1000 nm (0.8%). The percentages in parentheses are the relative deviation from targeted values. The rod dimensions are $r_1 = 202$ nm (-3%) and $r_2 = 424$ nm (1.7%). The walls have $t_{\text{thick}} = 241$ nm (1.2%) and $t_{\text{thin}} = 385$ nm (3%). Additional PWEM simulations were performed using the measured dimensions to find n_{thick} and n_{thin} for actual devices. For z - and y -polarized light, Δn_{eff} was found to be 0.0725 and 0.0584, which by Eq. 5.4 gives expected values of $f = 97$ μm and 120 μm , respectively.

5.3.2. Fresnel-Binary-Lens-Embedded photonic crystals

To explore the performance of F-B-LEPCs, the series shown in Figure 5.3a(1-3) were fabricated and characterized. As designed, the devices differ only in length of the lensing regions *before* phase wrapping. The F-B-LEPCs have $L_x = 71a$, $1.5 \times 71a$, and $2 \times 71a$, so by Eq. 5.4 their focal power should increase down the series. All devices were phase wrapped to the same L_{FB} , so the strongest-focusing device has the fastest phase wrapping and the most phase zones. The walls and rods were exposed as described above. Thin-wall unit cells were found to shrink 1.5% more than thick-wall unit cells, and the wall-thickness changes abruptly where phase wraps. So to minimize distortions, a_x was increased by 1.5% for thin-wall unit cells. Measurements from SEM images show that structural parameters like a , t_{thin} , and t_{thick} match those of the B-LEPC to within 1%, so Δn_{eff} must be similar.

5.4. Optical characterization results and analysis

5.4.1. Optical characterization results for Binary-Lens-Embedded photonic crystals

The LEPCs were optically characterized using a scanned-optical-fiber system (Figure 5.1(b)) described in [59], and the data were analyzed using methods detailed in [16]. A brief description is repeated here to provide context for the present work. Single-mode optical fibers (Thorlabs 1550BHP) are used to couple light into the LEPC and observe how light propagates after exiting. Light from source fiber (SF) propagates distance d_1 along \hat{x} as a gently diverging Gaussian beam [77] before entering the LEPC. Light exiting the device travels distance x where it

is sampled by a detection fiber (DF) coupled to a photodiode. The signal $S(x, y, z)$ is recorded as DF scans through the beam to obtain spatial intensity maps. The coordinate system is shown in Figure 5.1(b), and position $x = 0$ is located at the exit-face of the LEPC.

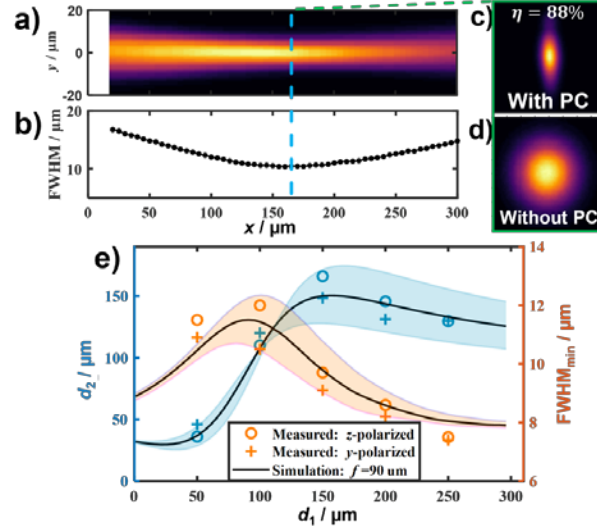


Figure 5.2: Optical characterization of B-LEPC seen in Figure 5.1(c). (a) xy -scan obtained with z -polarized light and $d_1 = 150$ μm . (b) FWHM versus x extracted from xy -scan. The focus and FWHM_{\min} appear at $x = d_2$ (blue dashed line) (c, d) Beam profiles obtained from yz -scans at $x = d_2$ with and without B-LEPC. (e) FWHM_{\min} and d_2 plotted versus d_1 for z - and y -polarized light.

Black curves and shaded regions give simulated FWHM_{\min} and d_2 for $f = 90$ $\mu\text{m} \pm 5$ μm .

The positions of the SF, device, and DF are observed with an optical microscope and images are used to confirm values of d_1 and d_2 . Scans of S within a yz -plane are used to observe the transverse profile of the beam at a given x . Scans in the xy -plane reveal how the beam changes as it propagates along \hat{x} , and the width of $S(x)$ is taken as its full-width at half-maximum

(FWHM). The FWHM of the beam itself is obtained by deconvoluting $S(x)$ from the impulse response function of DF. Conversely, the spatial profile of $S(x)$ can be modeled when the distribution of intensity and phase of the beam are specified.

Figure 5.2 shows results from optical characterization of the B-LEPC in Figure 5.1(c) when light is z -polarized. Figure 5.2(a) shows the xy -scan, from which $\text{FWHM}(x)$ was extracted to obtain Figure 5.2(b). After exiting the B-LEPC, the beam propagates in free space and its FWHM first narrows, reaches FWHM_{\min} at $d_2 = 157 \mu\text{m}$, then widens. Figure 5.2(c-d) show the transverse profile at d_2 . When the B-LEPC is present, the beam is much narrower along \hat{y} , providing clear evidence of cylindrical focusing. The power throughput η was calculated as the ratio of integrated energy collected in transverse scans with and without the B-LEPC. Scaling for collection efficiency [16] gives $\eta = 88\%$.

The focal length f was found by analyzing multiple sets of d_2 and FWHM_{\min} measured versus d_1 . The focal length cannot be taken as d_2 alone because the SF produces a diverging beam (Rayleigh range = $67 \mu\text{m}$) whose curvature and spot-size at the input to the LEPC affects the focusing. Scans like those in Figure 5.2(a-b) were repeated at $d_1 = 50 \mu\text{m}$, $100 \mu\text{m}$, $150 \mu\text{m}$, $200 \mu\text{m}$, and $250 \mu\text{m}$ for both y - and z -polarized light and used to obtain FWHM and d_2 , shown in Figure 5.2(e). These can be compared to simulated values (*black curves*) obtained by numerically propagating a Gaussian input beam distance d_1 from SF and focusing with a *thin lens* having $f = 90 \mu\text{m}$ [16]. The shaded region indicates the change in focusing when f varies by $\pm 5 \mu\text{m}$. The experimentally measured d_2 (*blue*) and FWHM_{\min} (*orange*) follow the trend of the simulation [78], indicating that the B-LEPC behaves like a thin lens. The focal length was extracted using linear

regression [16] and found to be $93 \mu\text{m} \pm 3 \mu\text{m}$ and $94 \mu\text{m} \pm 2 \mu\text{m}$ for y - and z -polarized light, respectively.

5.4.2. Optical characterization results for Fresnel-Binary-Lens-Embedded photonic crystals

Figure 5.3 shows data obtained from optical characterization of the F-B-LEPCs. As L_x increases, the FWHM_{min} shifts toward the device and the focal spot narrows, consistent with increasingly stronger focusing. Down the series, the focal lengths for z - and y -polarized light respectively are $94 \mu\text{m} \pm 2 \mu\text{m}$ and $93 \mu\text{m} \pm 3 \mu\text{m}$; $67 \mu\text{m} \pm 1 \mu\text{m}$ and $65 \mu\text{m} \pm 1 \mu\text{m}$; and $48 \mu\text{m} \pm 1 \mu\text{m}$ and $43 \mu\text{m} \pm 1 \mu\text{m}$. Note as L_x increases by $\times 1.5$ and $\times 2$, f decreases by $\times 1.5$ and $\times 2$ times, in agreement with Eq. 5.4. Down the series, the throughput η was found to be 85%, 83%, and 76%. As focusing getting stronger, η becomes smaller, which may be due to increased scattering from increasing phase wrapping. A F-B-LEPC like that in Figure 5.3(a1) was also fabricated without compensating for shrinkage. No significant changes in focusing or η were observed, suggesting the properties of F-B-LEPCs are robust even with some deformation. The strongest focusing F-B-LEPC in Figure 5.3(a3) has $NA = 0.59$.

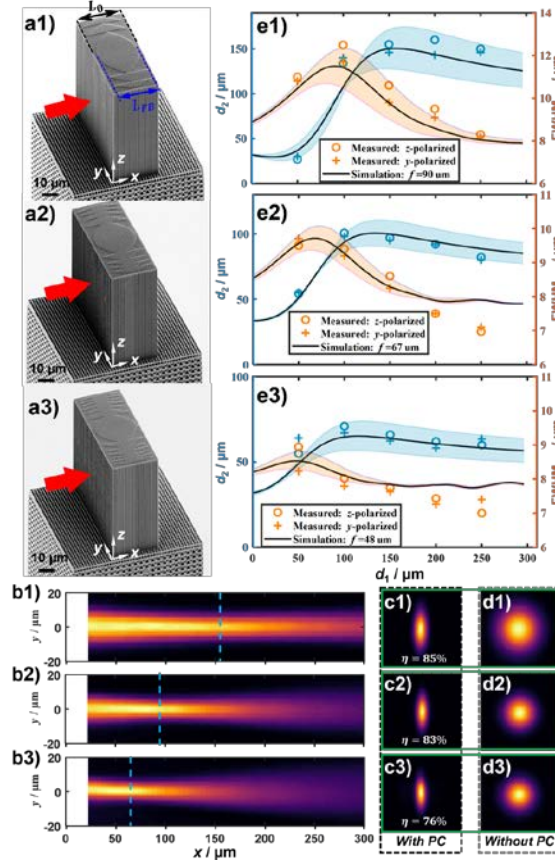


Figure 5.3: Fresnel B-LEPCs designed to have identical *physical* length L_0 but increasingly faster phase wrapping for tighter focusing. Without phase wrapping, the *effective* length of the lensing region (L_x) is (#1) $71a$, (#2) $1.5 \times 71a$, and (#3) $2 \times 71a$. (a1 - a3) SEM images of the F-B-LEPCs. (b1 - b3) xy -scans with $d_1 = 150 \mu m$ and z -polarized light. Dashed blue lines indicate the apparent focus at $x = d_2$. (c1 - c3, d1 - d3) Transverse scans in the focal plane with and without the F-B-LEPC. (e1 - e3) $FWHM_{min}$ (orange) and d_2 (blue) plotted versus d_1 for z - and y -polarized light. Note the change in scale of the vertical axes.

Three observations suggest that B-LEPCs perform the same after phase-wrapping. Note that by design, the first F-B-LEPC in Figure 5.3 differs from the B-LEPC of Figure 5.1 and Figure 5.2 only in having wrapped phase. Comparing Figure 5.2(a) and Figure 5.3(a1) shows the two LEPCs produce similar xy -scans with similar d_2 . This was also true for scans performed at other d_1 . Also, both have the same f and η , within 3%.

5.4.3. Simulation results for the Fresnel-Binary-Lens-Embedded photonic crystal

The propagation of light within the F-B-LEPCs was simulated using the finite-difference time-domain method (FDTD) [83]. Periodic boundary conditions were applied to simulate a device one unit cell thick along \hat{z} . The incident beam was a z -polarized planewave along \hat{z} and a diverging Gaussian along \hat{y} that originated at $d_1 = 150 \mu\text{m}$ with the mode field diameter of $9.5 \mu\text{m}$, like that measured at the exit of the source fiber (SF). Perfectly matched layers were applied at the perimeters along \hat{x} and \hat{y} . In units of pixels/ μm , the resolution was 80, 80, and 40 along \hat{x} , \hat{y} , and \hat{z} , respectively. Convergence was verified by increasing spatial resolution and time steps. The propagation of light after exiting the lattice was simulated using the beam-propagation method (BPM).

Results from the simulation of the F-B-LEPC seen in Figure 5.3a(1) are presented in Figure 5.4. The input beam has a convex wavefront initially. As it travels through the lattice, the lensing region reshapes the wavefront making it concave at the exit, consistent with design. From Figure 5.4c, the FWHM_{\min} occurs at $d_2 = 153 \mu\text{m}$, in agreement with the experiment of Figure

5.3(e1). Note that the experimental xy -scan is broader and smoother because it is a convolution of beam-intensity with the point-spread function of the DF.

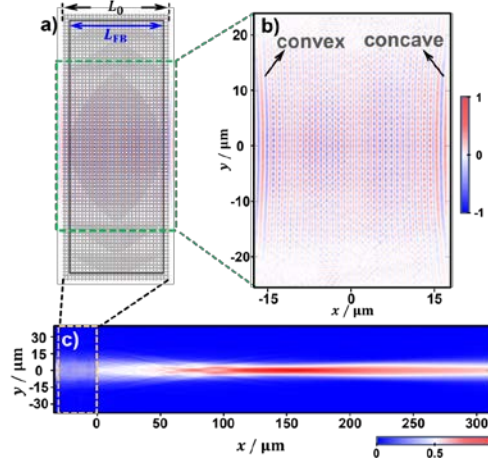


Figure 5.4: Simulation of a Gaussian beam coupled into a F-B-LEPC. (a) The structure's geometry matches the fabricated device in Figure 5.3(a1). (b) E_z -field in region identified with green-dashed line. (c) Normalized irradiance as $|E_z|^2$ within and after exiting the PC.

5.5. Summary

The B- and F-B-LEPCs have three inherent advantages over the conventional refractive micro-lenses. 1) Δn_{eff} can be adjusted using geometric properties rather than just material properties. 2) SC enables the device to function like a thin lens, even when NA is large. 3) The thickness of the LEPC can be adjusted without affecting the profile of the lensing region or focusing that results.

B- and F-B-LEPC may be useful for fiber-to-chip and chip-to-chip interconnects. Additionally, other phase profiles may also be added to the PCs to make mode converters and other

multi-functional devices to further reduce the footprint of integrated circuits. The LEPCs may also be candidates for some imaging and sensing applications.

6. LENSED-BENDER BASED ON SELF-COLLIMATING SPATIALLY-VARIANT PHOTONIC CRYSTALS

6.1. Introduction

Chapters 4-5 discussed the concept of using SC for independently controlling phase and power and demonstrated how it could be achieved experimentally with the use of a self-collimating lattice containing a GRIN lens, a binary lens, and a phase-wrapped Fresnel-type of binary lens. As light traverses the LEPCs, it accumulates a phase of parabolic shape, and the power of light is directed in the direction of self-collimation. In the LEPCs, only the phase is programmed, but not the power. Jennefir et al. demonstrated that it is possible to direct light through a 90° turn [51]. The direction of power flow in the bender is gradually altered as light passes through, but the phase is not actively changed. The LEPCs and the bender either programmed the profile of phase accumulated or the trajectory of power flow when light travels through the lattice.

This chapter discusses a lensed bender that is illustrated in Figure 6.1, where a lensed bender combines the capabilities of a lens and bender into a single device, thus reducing the footprint of optical devices. As light traverses through the lensed bender, phase accumulates a parabolic profile, and light is forced to flow in the bending direction due to SC. Inside and outside the yellow lensing region in Figure 6.1(c), the walls are thick and thin. To adapt a traditional lens for use in a bender, its shape must be transformed, and the lens profiles often need to be wrapped to make it fit in the bender. Benders and lensed benders like that shown in were fabricated by MPL in the photopolymer “IP-Dip” (Nanoscribe) [59], structurally characterized by SEM, and optically characterized using a home-build fiber-scanning system [16].

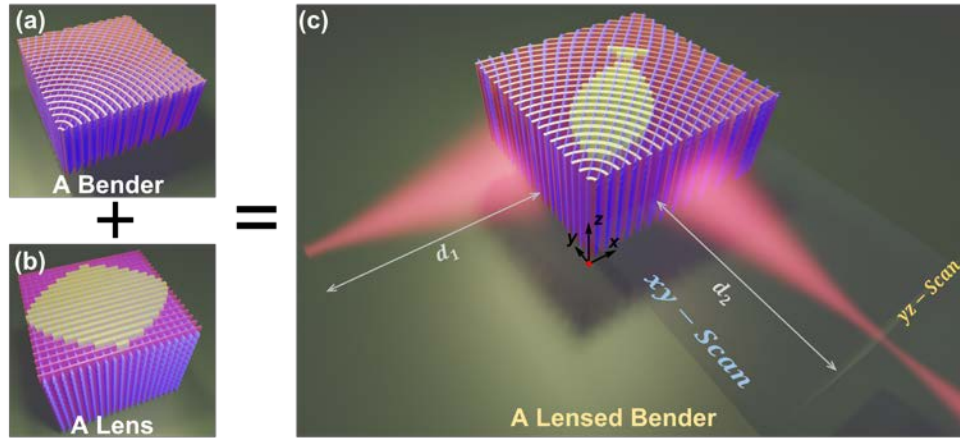


Figure 6.1: Design a (c) lensed bender by combining (a) a bender and (b) a lens

6.2. Design a binary-lens embedded bender

Figure 6.1(c) illustrates a lensed bender that is obtained by joining two benders. The two benders are constructed with the same unit cell and spatially variation maps of lattice spacing and orientation. However, they have different fill-factor (FF) maps, resulting in benders with thin and thick walls, respectively. The lensing region of the bender composed of thin walls will be replaced with the lensing region of the bender composed of thick walls to generate a lensed bender.

6.2.1. Generate benders

The benders are generated using a spatially-variant lattice (SVL) algorithm developed by Rumpf et al. [73]. As inputs, the algorithm requires a gray scale unit cell and three spatial variation maps that include periodicity, orientation, and the fill-factor (FF). An analog lattice of the gray

scale unit cell will first be generated using the input maps of periodicity and orientation. Next, the FF map will be used to threshold the variation of the unit cell locally and to produce a binary SVL.

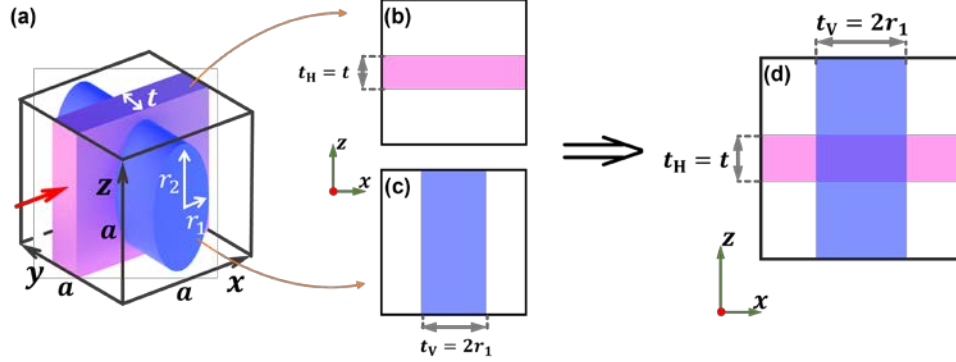


Figure 6.2: (a) The 3D unit cell consists of an elliptical rod intercepting a wall. The two parameters that need to be spatially varied are t and $2r_1$, which are translated into (b) H- and (c) V-bar, separately, which are then used to compose a (d) 2D unit cell for spatial variation.

The benders and lensed benders are based on the unit cell in Figure 6.2(a), which is the same unit cell used to compose the GRIN-, B-, and F-B-LEPCs. This unit cell is defined by three structural parameters, the wall thickness t , and the short (r_1) and long (r_2) axes of the elliptical rod. SVL algorithm is used to generate benders and lensed benders using the 3D unit cell. Once the SVLs have been generated, they will be transformed into G-code for fabrication.

Intuitively, a 3D SVL would be generated from the 3D SVL algorithm. Yet, spatially varying 3D unit cells is time consuming, particularly when the lattice size is large, and a high spatial resolution is required. The problem can be mitigated by translating the 3D unit cell in Figure 6.2(a) into the 2D unit cell in Figure 6.2(d). The 2D unit cell is then used for spatial variation and to generate G-code.

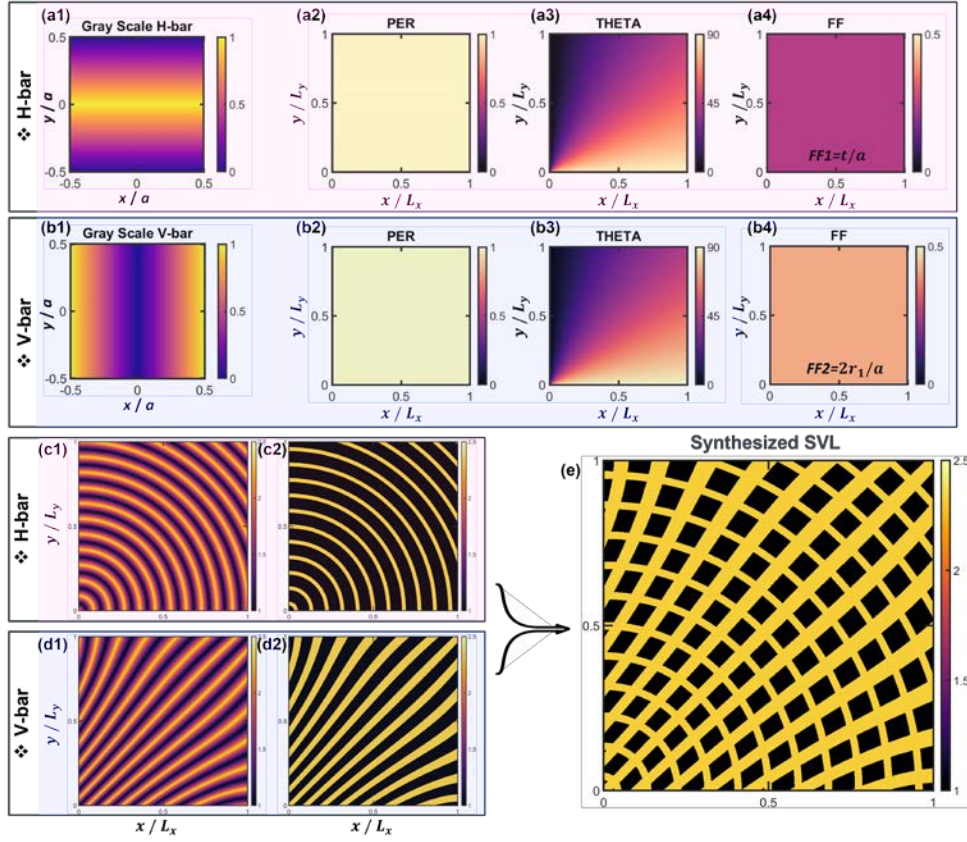


Figure 6.3: Gray-scale unit cells and the maps for generating a 90° bend. (a1) and (b1) are gray scale unit cells for a H- and V-bar, respectively. a(2-4) and b(2-4) are two sets of input maps containing period, angle, and fill-factor for separately spatially vary the H- and V-bar. The generated analogue and binary SVLs containing 11×11 unit cells generated from the H- and V-bar are shown in (c1) and (c2), and (d1) and (d2), respectively. (e) Synthesized lattice from combining (c2) and (d2).

When generating a bender and a lensed bender, it is necessary to vary the lattice orientation and FF only along the xy -plane and not in the z -axis. Therefore, only structural parameters t and $2r_1$ need to be spatially varied, but not $2r_2$. The 3D unit cell in Figure 6.2(a) can be translated into

the 2D unit cell in Figure 6.2(d) by converting the wall into a horizontal bar (H-bar) having thickness $t_H = t$ in and a vertical bar (V-bar) of thickness $t_V = 2r_1$, as shown in Figure 6.2 (b) and (c), respectively.

The H- and V-bars of the 2D unit cell in Figure 6.2(d) are spatially varied separately and then combined to generate a SVL, shown in Figure 6.3(e). Gray scale unit cells containing only the H- and V-bar shown in Figure 6.3 (a1) and (b1), along with their spatial variation maps in Figure 6.3a(2-3) are input to the SVL algorithm. The algorithm outputs analogue SVLs of the H- and V-bar and are shown in Figure 6.3(c1) and Figure 6.3(d1), respectively, under the spatial resolution of 60 pixel/ unit cell. The FF maps in Figure 6.3(a4) and (b4) are subsequently used to threshold the analogue SVLs and to generate binary SVLs that contain the correct thicknesses of the H- and V-bar, and are illustrated in Figure 6.3(c2) and Figure 6.3(d2), respectively. The two binary SVLs are then combined to produce the 2D SVL, as shown in Figure 6.3(e).

The previously described step will be used to generate two sets of 2D SVLs having the same inputs of unit cell and maps of spacing and orientation, but FF1 is set to t_{thin}/a and t_{thick}/a , respectively. The two sets of SVLs containing walls of two thicknesses will be combined together to generate lensed benders like that shown in Figure 6.1(c).

6.2.2. Generate lensed benders

The profile of a lens embedded in a normal lattice, as shown in Figure 6.4(a), needs to be translated when embedded in a bender, as shown in Figure 6.4(b). In Figure 6.4(a), the width L_x and height L_y of the lens determine the shape and focusing power of the lens. Half the height of

the lens is denoted by d and equals to $L_y/2$. A lens profile is transformed into a bender based on the principle that the optical path difference (OPD) experienced by light from traveling inside of the lensing region should not change. Before transformation, the length of the lensing region $t(y)$ is given in Eq. (6.1)

$$t(y) = L_x \left(1 - \frac{y^2}{d^2}\right), \quad (6.1)$$

and $t(y)$ parabolically decreases from L_x in the center ($y = 0$) to 0 at the side ($y = d$). The lens is transformed into a bender bigger than the size of the lens, and the bottom tip of the lens is r_0 away from the rotation center of the bender as illustrated in Figure 6.4(b). The thicknesses $t(y)$ inside a bender is given by

$$t(y) = 2(r - r_0)\theta, \quad (6.2)$$

where θ is the angle between the center of the lens and the line from the bottom tip of the lens to point P, and P denotes a point on the boundary of the lens that is y distance away from the center. Combine Eq. (6.1) and Eq. (6.2) gives

$$\theta = \frac{L_x}{2d^2} \frac{d^2 - (r-d)^2}{r-r_0}, \quad (6.3)$$

Then the coordinates of $P_1(x_{p1}, y_{p1})$ is given by

$$x_{p1} = r_0 \cos\left(\frac{\pi}{2}\right) + (r - r_0) \cos\left(\theta + \frac{\pi}{2}\right), \quad (6.4)$$

$$y_{p1} = r_0 \sin\left(\frac{\pi}{2}\right) + (r - r_0) \sin\left(\theta + \frac{\pi}{2}\right). \quad (6.5)$$

Similarly, the coordinates of $P_2(x_{p2}, y_{p2})$ can be solved by replacing θ with $-\theta$ into Eq. (6.4) and Eq. (6.5).

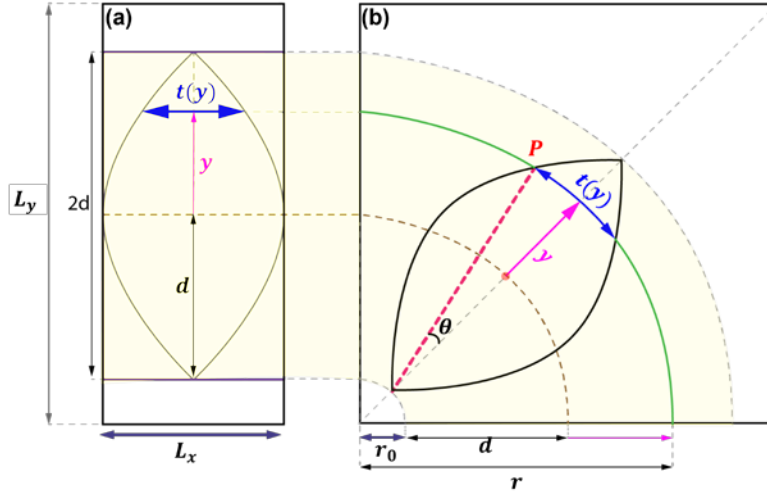


Figure 6.4: Translating a lens profile from embedding inside of (a) a normal lattice to inside of (b) a bender

6.2.3. Generating G-code for fabrication

A G-code contains two pieces of information, the path coordinates, and the power for exposure, which can be determined from the analogue and binary SVLs, respectively. The coordinates of the H- and V-bar can be determined by locating the local minima from their respective analogue SVLs and grouping them into the correct order of lines. The extracted coordinates for the H- and V-lines are depicted with black lines in Figure 6.5 (a1) and (a2), respectively. To ensure that light passes through an integer number of unit cells when traversing through a bender and lensed bender, lines that extend beyond a full unit cell must be removed. This is done by finding the points where the central lines of the H- and V-bar cross, as shown with dots in Figure 6.5 (b1) and (c1), respectively. The part of lines extending beyond the cross points will then be eliminated.

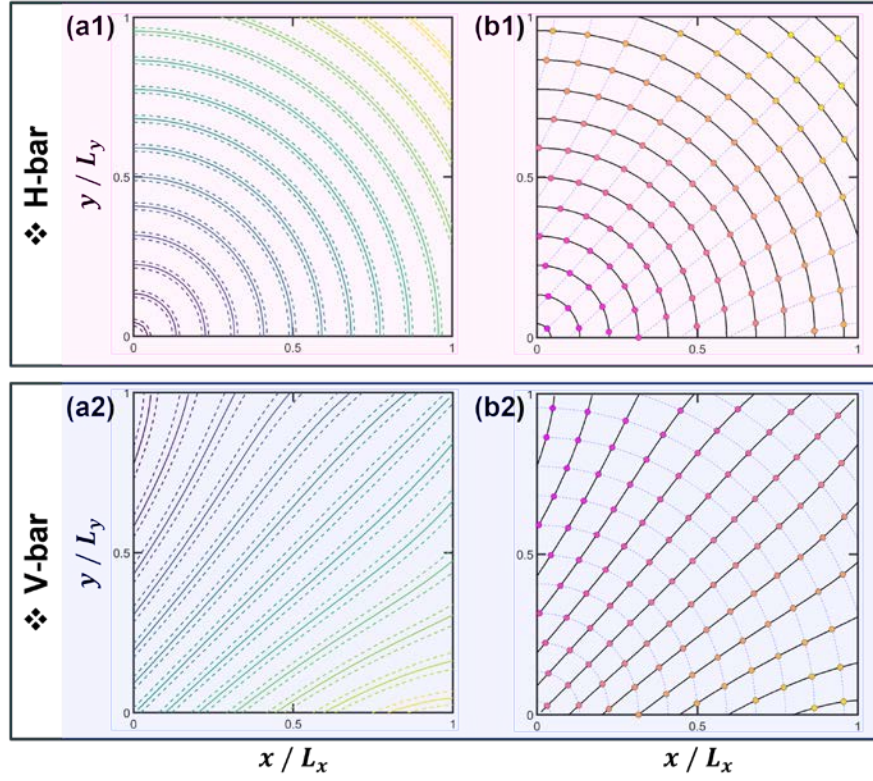


Figure 6.5: Center (solid) and contour (dash) lines of the (a1) H-bars and (a2) V-bars. Grouped points that define coordinates for the (b1) H- and (b2) V-bars. The points are where the central lines of the H- and V-bar cross.

Powers to be used for exposure of the H- and V-bar are found from the contour lines shown in Figure 6.5 (a1) and (a2), respectively. At each cross point, the exposure power is determined by finding the voxel size that is tangent to both contour lines that contain the cross point. The coordinates and the powers are then combined to generate G-code for patterning benders and lensed benders.

6.3. Fabrication and structural characterization

6.3.1. Bender

The bender in Figure 6.6 is designed to have $L_x = L_y = L_z = 71a$. SEM images like those in Figure 6.6(b-c) were used to determine the geometrical parameters. The unit cell spacings perpendicular to the bending-direction and z-directions are 963 nm and 970 nm, exceeding the targeted periodicity of 992 nm by 2.9% and 2.5%. The periodicity along the bending direction is not a constant and varies with the bending radius r . Three measurements were taken at three points along an arc, compared to the dimensions as designed, and the average error is calculated to be 2.3%. The wall thickness was measured to be 282 nm. The long axis of the elliptical rods is measured to be 445 nm, which is 2.7% from the targeted dimension. The short axis is measured at the same locations where the periodicities along the bending-direction were measured, and the average error is calculated to 2.8%.

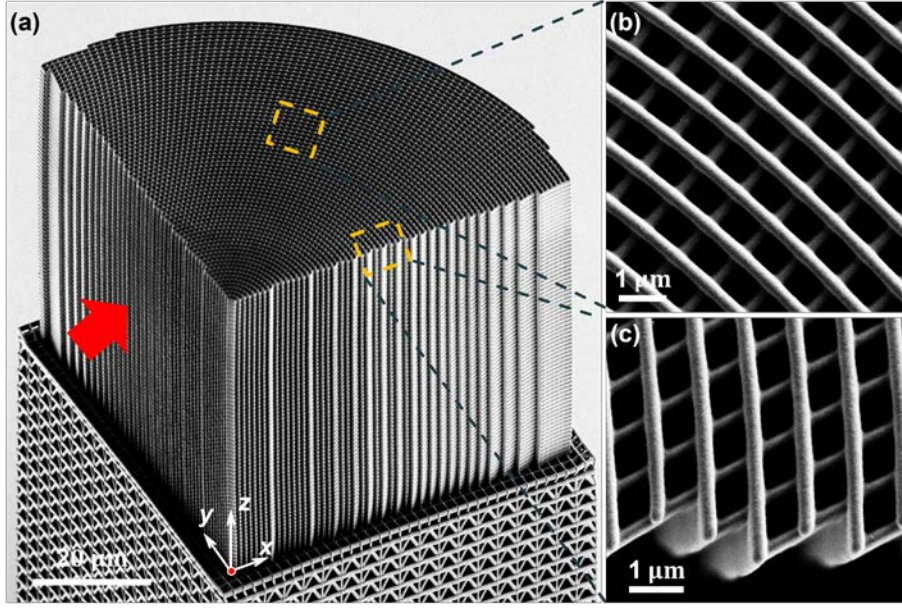


Figure 6.6: SEM images of a bender having $71 \times 71 \times 71$ unit cells. (a) Side-view of the whole lattice. Zoomed-in top view at the (b) middle and the exit side of the lattice. Light is chosen to incident along the direction of the red arrow.

6.3.2. Lensed bender

The lensed-bender in Figure 6.6(a) is designed to have $L_x = L_y = L_z = 71a$. SEM images like those in Figure 6.7(b-c) were used to determine the geometrical parameters and found to match the targeted dimensions within experimental error. The unit cell spacings perpendicular to the bending-direction and z-directions are 1010 nm and 980 nm, exceeding the targeted periodicity of 992 nm by 1.7% and 1.2%. The periodicity along the bending direction was measured at the same locations as that of the bender in Figure 6.6(a), and the average error is calculated to be 1.3%. The wall thicknesses for the thin and thick walls were measured to be 270 nm and 409 nm, and the

$\delta t/a$ is calculated to be 0.137, which is 1.5% off from the targeted. The long axis of the elliptical rods is measured to be 455 nm (3.7% off). The short axis is measured using at the same locations as that when measuring periodicities along the arc direction, and the average error is calculated to be 2.5% off. The experimental parameters were put into PWEM simulation to recalculate the δn_{eff} and is found to be 0.0693. The expected focal length (f_{expected}) is calculated to be 125 μm .

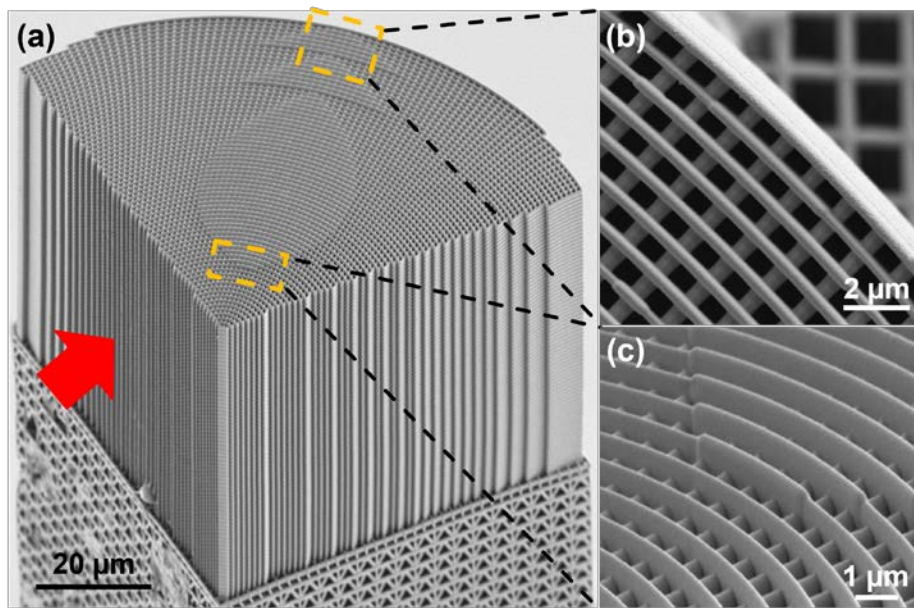


Figure 6.7: SEM images of a lensed-bender having $71 \times 71 \times 71$ unit cells. (a) Side-view of the whole lattice. Zoomed-in view from the (b) top and the (c) side. Light is chosen to incident along the direction of the red arrow.

6.4. Optical characterization results and analysis

6.4.1. Optical characterization results for Benders

The bending performance is dependent on the radius of the bending path r . To map out the bending performance of bending versus r , the SF is scanned along the y -axis from the bottom to the top of the bender with d_1 fixed to $100\text{ }\mu\text{m}$ with the step size of $20\text{ }\mu\text{m}$, and the corresponding spot size is $13\text{ }\mu\text{m}$ when light is incident on the entrance face of the bender.

The xy -scans when the SF is positioned in Figure 6.8a(1-4) are shown in Figure 6.8b(1-4) and Figure 6.8d(1-4), respectively, for the z - and y -polarized light. From the xy -scans, the FWHM is extracted at each y -location and is plotted in Figure 6.8c(1-4) and Figure 6.8e(1-4), respectively, for the z - and y -polarized light.

For both polarization states, the beam width before and after exiting the lattice is relatively unchanged as shown in Figure 6.8c(1-4) and Figure 6.8e(1-4). The highest bending efficiency for the z -polarized light is achieved when the SF is close to the rotation center and is found to be 6.4%. The bending efficiency for the y -polarized light, however, is even lower. The xy -scans shown in Figure 6.8d(1-4) for the y -polarized light is unstable. This is potentially due to the limited acceptance angle of SC for the y -polarized light.

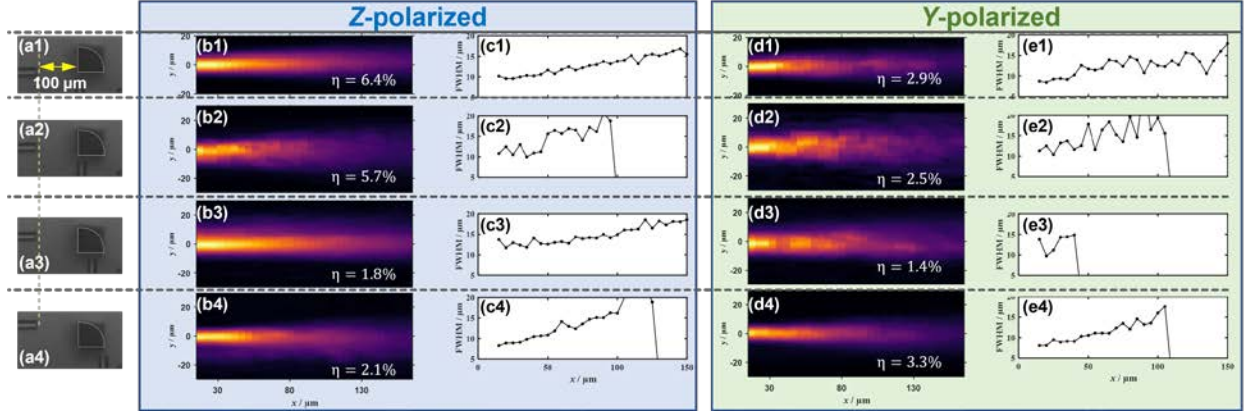


Figure 6.8: Optical characterization of the bender seen in Figure 6.6(a). a(1-4) are optical microscope images when the SF is scanned from the bottom to the top of the lensed-bender along the y -axis, with the step size of $20\text{ }\mu\text{m}$ and $d_1 = 100\text{ }\mu\text{m}$. The xy -scans of the SF at those locations are shown in b(1-4) and d(1-4) for the z - and y -polarized light, respectively. The FWHM at each y -location is extracted from b(1-4) and d(1-4), and are shown in c(1-4) and e(1-4), respectively.

6.4.2. Optical characterization results for Lensed Benders

The optical characterization results for the z - and y -polarized light of the lensed bender in Figure 6.6 is shown in Figure 6.7. The SF was positioned $50\text{ }\mu\text{m}$, $100\text{ }\mu\text{m}$, $150\text{ }\mu\text{m}$, $200\text{ }\mu\text{m}$, and $250\text{ }\mu\text{m}$ from the front surface of the lensed-bender, and the distances are verified from the optical microscopy images shown in Figure 6.7a(1-5). At those d_1 distances, the transverse beam profiles at the exit side along the xy -plane were revealed with xy -scans, shown in Figure 6.7b(1-5) and Figure 6.7d(1-5), respectively, for the z - and y -polarized light. From the xy -plots, FWHM was

extracted at each y -location and the results are shown in Figure 6.7c(1-5) and Figure 6.7e(1-5), respectively, for the z - and y -polarized light.

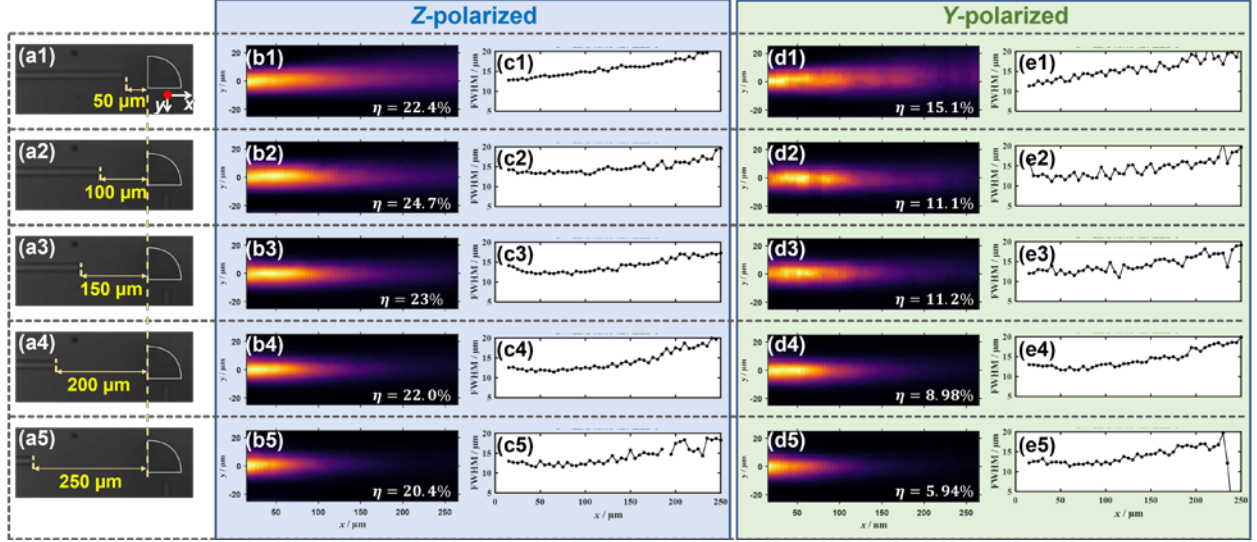


Figure 6.9: Optical characterization of the lensed-bender seen in Figure 6.6(a). a(1-5) are optical microscope images when d_1 is set to 50 μm , 100 μm , 150 μm , 200 μm , and 250 μm . At these d_1 locations, the xy -scans are shown in b(1-5) and d(1-5) for the z - and y -polarized light, respectively. The FWHM at each y -location is extracted from b(1-5) and d(1-5), and are shown in c(1-5) and e(1-5), respectively.

As the beam exits the lensed-bender, it propagates in air along the y -axis without being angled. Its FWHM narrows at first, reaches FWHM_{\min} at around 65 μm and then widens. This is a direct indication of focus. Experimentally, it is observed that d_2 remains unchanged when d_1 changes from 100 μm to 250 μm . If the lensed-bender behaves as a thin lens, noticeable changes in d_2 should be observed when d_1 is changed, since the Rayleigh range (67 μm) of the input beam

is compared to the f_{expected} . The focusing behavior of the lensed-bender does not match that of a Gaussian beam focused by a thin lens, implying that SC may not hold true when light propagates inside the lattice. This is indeed observed experimentally that the center of the exiting beam does not track that of the incident beam, but instead exits at centers of a larger radius than that of the incident beam. Consequently, the beam will walk off the bending path and encounter more of the lensing region, causing a strong focus. A y -polarized light exhibits a similar focusing behavior to a z -polarized light. The only difference is the power throughput (η). The η for the z -polarized light is averaged 23%, which is twice as high as that for the y -polarized light.

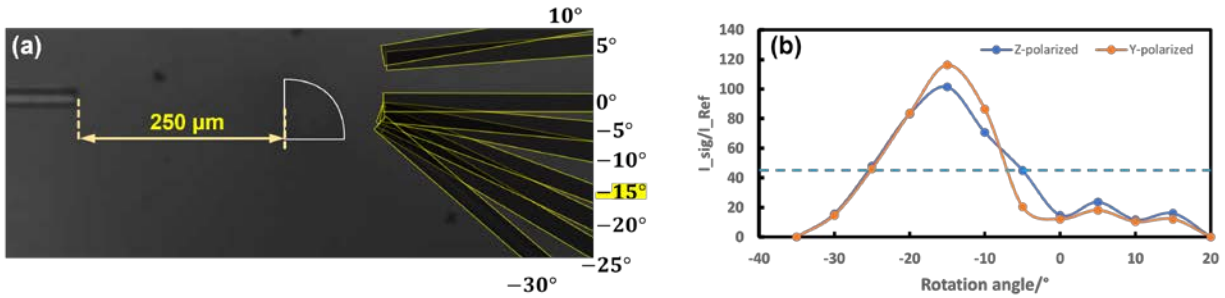


Figure 6.10: Detection of light not bent through the bender. (a) The DF is scanned from -30° to 10° with the step size of 5° when d_1 is set to $250 \mu\text{m}$. (b) Maximum signal strength versus the rotation angle. The blue line is a reference for light bent by 90° .

Low η can be attributed to reflections at the front surface, and scattering and insufficient bending of light as it passes through the lensed bender. Reflections from the front surface and scattering from the surface should not be the primary source of the power loss since the difference of the refractive index between the lattice and air is only 0.3. Also, the lattice is smooth, so

scattering is minimized. It is reasonable to assume that the power loss is mainly caused by insufficient bending.

To study the behavior of the light coming from the curving side of the lattice due to insufficient bending, the DF was angled from -30° to 10° with a step size of 5° , and d_1 is set to $250\text{ }\mu\text{m}$, as shown in Figure 6.8(a). At each angle, the DF was scanned around the yz -plane to find the maximum signal level, and the results are shown in Figure 6.8(b). For both the z - and y -polarized light, intensity peaks at -15° . With this angle, the peak intensity is twice as large as when the light travels through the bender. Accordingly, most of the light is lost due to insufficient bending.

6.5. Summary

This chapter describes the design, fabrication, and characterization of a lensed bender based on the SVPC. It was demonstrated through optical characterization that it is indeed possible to combine two optical functions, bending and focusing, in one device. The lensed bender, however, has a throughput of only 24%, due to insufficient bending strength. We think this is primarily due to the quality and robustness of the SC against spatial variation. There are three possible ways to improve bending efficiency. First, keep the original unit cell and reduce the bending angle so that SC is better preserved. Second, keep the original unit cell and increase the refractive index of the composite material. This can be achieved by using resins with a higher refractive index after photopolymerization. Third, explore other unit cells having better acceptance

angles for SC. Lensed benders may be applied to integrated photonic devices to further reduce their footprint.

7. SUMMARY AND OUTLOOK

In summary, we achieved light guiding and concentrating based on self-collimating spatially-variant photonic crystals for independent power and phase control. We also proposed a general method for correctly calculating the refractive index of a Bloch mode in a PC by recovering the lost band folding information. The concept is proved in simulation and experiment through devices like 3D hexagonal lattices and lens-embedded photonic crystals.

In Chapter 3, we demonstrated the possibility of molding the flow of light using SC achieved in a 3D volumetric hexagonal PC fabricated with a low-refractive-index photopolymer. Experimentally, we showed that light can be coupled into the hexagonal PC with an input angle of up to 50° and the input wavelength from 1360 nm to 1610 nm.

In Chapter 4, we proposed the concept that PCs can be engineered so that the flow of optical power and the phase of the field can be independently controlled. The concept is demonstrated by creating a self-collimating lattice with an embedded cylindrical lens. The device is fabricated in a low-index photopolymer using MPL with the lattice spacing chosen for operation around the telecom wavelength of 1550 nm. The lattice is based on a low-symmetry rod-in-wall unit cell that strongly self-collimates light. The walls are varied in thickness to modulate the effective refractive index so light acquires a spatially quadratic phase profile as it propagates through the device. Although the phase of the field is altered, the light does not focus within the device because SC forces power to flow parallel to the principal axes of the lattice. Upon exiting the device, ordinary propagation resumes in free space and the curved phase profile causes the light to focus. An

analysis of the experimentally observed optical behavior shows that the device behaves like a thin lens, even though the device is considerably thick.

In Chapter 5, a binary-lens-embedded photonic crystal (B-LEPC) was designed for operation at 1550 nm and fabricated by MPL. The lens is binary in the sense that the optical path difference is generated using unit cells having just two distinct fill factors. The unit cell is the same as that in Chapter 4. Simulations show that SC forces light to move through the device without diffracting or focusing, even as the wavefront is reshaped by the lensing region. Upon exiting the device, the curved wavefront causes the light to focus. The thickness of a B-LEPC was reduced threefold by wrapping phase in the style of a Fresnel lens. Embedding a faster-varying phase profile enables tighter focusing, and $NA = 0.59$ was demonstrated experimentally.

In Chapter 6, a Fresnel type of binary lens is embedded into a 90° bender based on spatially-variant photonic crystal. The device was designed for operation at 1550 nm and fabricated by MPL. The device combines the optical functions of light bending and focusing into one device. The unit cell used to compose the lensed bender is the same that used in Chapter 4. Experimentally, it was observed that such devices bend and focus light. The throughput of the device is 24% due to insufficient bending power which is related to quality and robustness of the SC against spatial variation. The performance of the device should be improved by optimizing the SC of the current employed unit cell or finding other unit cells.

The B- and F-B-LEPCs have three inherent advantages over the conventional refractive micro-lenses. 1) Δn_{eff} can be adjusted using geometric properties rather than just material properties. 2) SC enables the device to function like a thin lens, even when NA is large. 3) The

thickness of the LEPC can be adjusted without affecting the profile of the lensing region or focusing that results. LEPC may be useful for fiber-to-chip and chip-to-chip interconnects. Additionally, other phase profiles may also be added to the PCs to make mode converters and other multi-functional devices to further reduce the footprint of integrated circuits. The LEPCs may also be candidates for some imaging and sensing applications.

APPENDIX A: COPYRIGHT PERMISSION LETTERS

Copyright letter from the Optica Publishing Group

Dear Chun Xia,

Thank you for contacting Optica Publishing Group.

For the use of figure 1 from Jesus J. Gutierrez, Noel P. Martinez, and Raymond C. Rumpf, "Independent control of phase and power in spatially variant self-collimating photonic crystals," J. Opt. Soc. Am. A 36, 1534-1539 (2019). Optica Publishing Group considers your requested use of its copyrighted material to be Fair Use under United States Copyright Law. We request that a complete citation of the original material be included in any publication.

For the use of material from Chun Xia, Stephen M. Kuebler, Noel P. Martinez, Manuel Martinez, Raymond C. Rumpf, and Jimmy Touma, "Wide-band self-collimation in a low-refractive-index hexagonal lattice," Opt. Lett. 46, 2228-2231 (2021) and Chun Xia, Jesus J. Gutierrez, Stephen M. Kuebler, Raymond C. Rumpf, and Jimmy Touma, "Cylindrical-lens-embedded photonic crystal based on self-collimation," Opt. Express 30, 9165-9180 (2022):

Because you are the author of the source paper from which you wish to reproduce material, Optica Publishing Group considers your requested use of its copyrighted materials to be permissible within the author rights granted in the Copyright Transfer Agreement submitted by the requester on acceptance for publication of his/her manuscript. We request that a complete citation of the original material be included in any publication. This permission assumes that the material was not reproduced from another source when published in the original publication.

While your publisher should be able to provide additional guidance, we prefer the below citation formats:

For citations in figure captions: [Reprinted/Adapted] with permission from [ref #] © The Optical Society. (Please include the full citation in your reference list). For images without captions: Journal Vol. #, first page (year published) An example: Biomed. Opt. Express 6, 793 (2015)

Please let me know if you have any questions.

Kind Regards,

Hannah Greenwood

April 5, 2022

Authorized Agent, Optica Publishing Group

APPENDIX B: PUBLIC RELEASEMENT STATEMENT

Distribution A - Approved for public release. Distribution Unlimited (AFRL-2022-2587).

APPENDIX C: LIST OF PUBLICATIONS

- 1) C. Xia, E. Bustamante, S. M. Kuebler, R. C. Rumpf, and J. Touma, "Binary-lens-embedded photonic crystals," under review.
- 2) C. Xia, S. M. Kuebler, N. P. Martinez, M. Martinez, R. C. Rumpf, and J. Touma, "Wide-band self-collimation in a low-refractive-index hexagonal lattice," *Opt. Lett.* 46, 2228-2231 (2021).
- 3) C. Xia, J. J. Gutierrez, S. M. Kuebler, R. C. Rumpf, and J. Touma, "Cylindrical-lens-embedded photonic crystal based on self-collimation," *Opt. Express* 30, 9165-9180 (2022).
- 4) C. Xia, S. Kuebler, N. Martinez, M. Martinez, R. Rumpf, and J. Touma, Wide-band self-collimation in low refractive index hexagonal lattice, *SPIE OPTO* (SPIE, 2022), Vol. 12010.
- 5) C. Xia, S. M. Kuebler, N. P. Martinez, M. Martinez, R. C. Rumpf, and J. Touma, "Experimental Demonstration Of Broadband Self-Collimation Effect In 3d Hexagonal Lattice Fabricated Using A Low-Refractive-Index Polymer," in *2020 IEEE Research and Applications of Photonics in Defense Conference (RAPID)*, (IEEE, 2020), 1-3.

REFERENCES

- [1] M. T. Bill Corcoran, Xingyuan Xu, Andreas Boes, Jiayang Wu, Thach G. Nguyen, Sai T. Chu, Brent E. Little, Roberto Morandotti, Arnan Mitchell & David J. Moss "Ultra-dense optical data transmission over standard fibre with a single chip source," *Nat. Commun.* **11**(2020).
- [2] K. I. Seo, B. Haran, D. Gupta, D. Guo, T. Standaert, R. Xie, H. Shang, E. Alptekin, D. I. Bae, and G. Bae, "A 10nm platform technology for low power and high performance application featuring FINFET devices with multi workfunction gate stack on bulk and SOI," in *2014 Symposium on VLSI Technology (VLSI-Technology): Digest of Technical Papers*, (IEEE, 2014), pp. 1-2.
- [3] W. J. Gallagher, E. Chien, T.-W. Chiang, J.-C. Huang, M.-C. Shih, C. Y. Wang, C. Bair, G. Lee, Y.-C. Shih, and C.-F. Lee, "Recent progress and next directions for embedded MRAM technology," in *2019 Symposium on VLSI Circuits*, (IEEE, 2019), pp. T190-T191.
- [4] "The zettabyte era: Trends and snalysis. Updated (07/06/2017)," (Cisco Systems, 2017).
- [5] N. Farrington and A. Andreyev, "Facebook's data center network architecture," in *2013 Optical Interconnects Conference*, (Citeseer, 2013), pp. 49-50.
- [6] Q. Cheng, M. Bahadori, M. Glick, S. Rumley, and K. Bergman, "Recent advances in optical technologies for data centers: A review," *Optica* **5**, 1354-1370 (2018).
- [7] R. Agarwal, J. Mudigonda, P. Yalagandula, and J. C. Mogul, "An algorithmic approach to datacenter cabling," **Hewlett-Packard Development Company, LP: Palo Alto, CA, USA**(2015).

- [8] C. Chaintoutis, B. Shariati, A. Bogris, P. V. Dijk, C. G. Roeloffzen, J. Bourderionnet, I. Tomkos, and D. Syvridis, "Free space intra-datacenter interconnects based on 2D optical beam steering enabled by photonic integrated circuits," in *Photonics*, (Multidisciplinary Digital Publishing Institute, 2018), 21.
- [9] J. H. Song, H. N. Fernando, B. Roycroft, B. Corbett, and F. H. Peters, "Practical design of lensed fibers for semiconductor laser packaging using laser welding technique," *J. Light. Technol.* **27**, 1533-1539 (2009).
- [10] S. Huang, S. Yeh, and W. Cheng, "A new scheme of conical-wedge-shaped fiber endface for high-power laser to single mode fiber coupling," in *Conference on Lasers and Electro-Optics*, (Optical Society of America, 2005), CWN2.
- [11] P.-I. Dietrich, M. Blaicher, I. Reuter, M. Billah, T. Hoose, A. Hofmann, C. Caer, R. Dangel, B. Offrein, and U. Troppenz, "In situ 3D nanoprinting of free-form coupling elements for hybrid photonic integration," *Nat. Photonics* **12**, 241-247 (2018).
- [12] V. R. Manfrinato, L. Zhang, D. Su, H. Duan, R. G. Hobbs, E. A. Stach, and K. K. Berggren, "Resolution limits of electron-beam lithography toward the atomic scale," *Nano letters* **13**, 1555-1558 (2013).
- [13] M. Grzelczak, J. Vermant, E. M. Furst, and L. M. Liz-Marzán, "Directed self-assembly of nanoparticles," *ACS nano* **4**, 3591-3605 (2010).
- [14] Q. Ge, Z. Li, Z. Wang, K. Kowsari, W. Zhang, X. He, J. Zhou, and N. X. Fang, "Projection micro stereolithography based 3D printing and its applications," *International Journal of Extreme Manufacturing* **2**, 022004 (2020).

- [15] M. Nakagawa, "Micro-print and nano-imprint methods combining laser-drilled screen printing and ultraviolet nanoimprint lithography: a review," *Japanese Journal of Applied Physics* (2022).
- [16] C. Xia, J. J. Gutierrez, S. M. Kuebler, R. C. Rumpf, and J. Touma, "Cylindrical-lens-embedded photonic crystal based on self-collimation," *Opt. Express* **30**, 9165-9180 (2022).
- [17] P. Danilevicius, S. Rekštyte, R. Gadonas, M. Malinauskas, E. Balciunas, R. Jarasiene, D. Baltriukiene, V. Bukelskiene, A. Kraniauskas, and R. Sirmenis, "Micro-structured polymer scaffolds fabricated by direct laser writing for tissue engineering," *Journal of biomedical optics* **17**, 081405 (2012).
- [18] J. Brown and W. Jackson, "The properties of artificial dielectrics at centimetre wavelengths," *Proceedings of the IEE-Part B: Radio and Electronic Engineering* **102**, 11-16 (1955).
- [19] A. Harvey, "Periodic and guiding structures at microwave frequencies," *IRE Trans. Microwave Theory Techniques* **8**, 30-61 (1960).
- [20] S. John, "Strong localization of photons in certain disordered dielectric superlattices," *Phys. Rev. Lett.* **58**, 2486-2489 (1987).
- [21] E. Yablonovitch, "Inhibited spontaneous emission in solid-state physics and electronics," *Phys. Rev. Lett.* **58**, 2059 (1987).
- [22] G. von Freymann, T. Y. Chan, S. John, V. Kitaev, G. A. Ozin, M. Deubel, and M. Wegener, "Sub-nanometer precision modification of the optical properties of three-dimensional polymer-based photonic crystals," *Photonics and Nanostructures-Fundamentals and Applications* **2**, 191-198 (2004).

- [23] G. Witzgall, R. Vrijen, E. Yablonovitch, V. Doan, and B. J. Schwartz, "Single-shot two-photon exposure of commercial photoresist for the production of three-dimensional structures," *Opt. Lett.* **23**, 1745-1747 (1998).
- [24] T. F. Krauss, R. M. Rue, and S. Brand, "Two-dimensional photonic-bandgap structures operating at near-infrared wavelengths," *Nature* **383**, 699-702 (1996).
- [25] J. D. Joannopoulos, S. G. Johnson, J. N. Winn, and R. D. Meade, *Photonic Crystals: Molding the Flow of Light* (Princeton University, 2008).
- [26] A. Mekis, J. Chen, I. Kurland, S. Fan, P. R. Villeneuve, and J. Joannopoulos, "High transmission through sharp bends in photonic crystal waveguides," *Phys. Rev. Lett.* **77**, 3787 (1996).
- [27] J. C. Knight, "Photonic crystal fibres," *Nature* **424**, 847-851 (2003).
- [28] S. Li, H. Lin, F. Meng, D. Moss, X. Huang, and B. Jia, "On-demand design of tunable complete photonic band gaps based on bloch mode analysis," *Sci. Rep.* **8**, 14283 (2018).
- [29] A. H. Safavi-Naeini and O. Painter, "Design of optomechanical cavities and waveguides on a simultaneous bandgap phononic-photonic crystal slab," *Opt. Express* **18**, 14926-14943 (2010).
- [30] E. Cubukcu, K. Aydin, E. Ozbay, S. Foteinopoulou, and C. M. Soukoulis, "Negative refraction by photonic crystals," *Nature* **423**, 604-605 (2003).
- [31] T. Baba, "Slow light in photonic crystals," *Nat. Photonics* **2**, 465-473 (2008).
- [32] H. Kosaka, T. Kawashima, A. Tomita, M. Notomi, T. Tamamura, T. Sato, and S. Kawakami, "Superprism phenomena in photonic crystals," *Phys. Rev. B* **58**, R10096 (1998).

- [33] H. Kosaka, T. Kawashima, A. Tomita, M. Notomi, T. Tamamura, T. Sato, and S. Kawakami, "Self-collimating phenomena in photonic crystals," *Appl. Phys. Lett.* **74**, 1212-1214 (1999).
- [34] J. J. Gutierrez, N. P. Martinez, and R. C. Rumpf, "Independent control of phase and power in spatially variant self-collimating photonic crystals," *J. Opt. Soc. Am. A* **36**, 1534-1539 (2019).
- [35] J. Arlandis, E. Centeno, R. Polles, A. Moreau, J. Campos, O. Gauthier-Lafaye, and A. Monmayrant, "Mesoscopic self-collimation and slow light in all-positive index layered photonic crystals," *Phys. Rev. Lett.* **108**, 037401 (2012).
- [36] L. Wu, M. Mazilu, and T. F. Krauss, "Beam steering in planar-photonic crystals: from superprism to supercollimator," *J. Light. Technol.* **21**, 561 (2003).
- [37] M. Gumus, I. H. Giden, and H. Kurt, "Broadband self-collimation in C2 symmetric photonic crystals," *Opt. Lett.* **43**, 2555-2558 (2018).
- [38] M. Li, W. Li, H. Huang, J. Wang, Y. Li, A. Wu, Z. Sheng, X. Wang, S. Zou, and F. Gan, "All-angle quasi-self-collimation effect in a rod-type silicon photonic crystal," *IEEE Photonics J.* **7**, 1-8 (2015).
- [39] H. M. Nguyen, M. Dundar, R. Van Der Heijden, E. Van der Drift, H. Salemink, S. Rogge, and J. Caro, "Compact Mach-Zehnder interferometer based on self-collimation of light in a silicon photonic crystal," *Opt. Express* **18**, 6437-6446 (2010).
- [40] P. T. Rakich, M. S. Dahlem, S. Tandon, M. Ibanescu, M. Soljačić, G. S. Petrich, J. D. Joannopoulos, L. A. Kolodziejski, and E. P. Ippen, "Achieving centimetre-scale supercollimation in a large-area two-dimensional photonic crystal," *Nat. Mater.* **5**, 93-96 (2006).

- [41] C. Chen, A. Sharkawy, D. M. Pustai, S. Shi, and D. W. Prather, "Optimizing bending efficiency of self-collimated beams in non-channel planar photonic crystal waveguides," *Opt. Express* **11**, 3153-3159 (2003).
- [42] D. M. Pustai, S. Shi, C. Chen, A. Sharkawy, and D. W. Prather, "Analysis of splitters for self-collimated beams in planar photonic crystals," *Opt. Express* **12**, 1823-1831 (2004).
- [43] Z. Wu, K. Xie, H. Yang, P. Jiang, and X. He, "All-angle self-collimation in two-dimensional rhombic-lattice photonic crystals," *J. Opt* **14**, 015002 (2011).
- [44] Y. Xu, X. J. Chen, S. Lan, Q. Guo, W. Hu, and L. J. Wu, "The all-angle self-collimating phenomenon in photonic crystals with rectangular symmetry," *Journal of Optics A: Pure Applied Optics* **10**, 085201 (2008).
- [45] Y. Chuang and T. Suleski, "Complex rhombus lattice photonic crystals for broadband all-angle self-collimation," *J. Opt* **12**, 035102 (2010).
- [46] H. E. Williams, Z. Luo, and S. M. Kuebler, "Effect of refractive index mismatch on multi-photon direct laser writing," *Opt. Express* **20**, 25030-25040 (2012).
- [47] T. Baldacchini, *Three-dimensional microfabrication using two-photon polymerization: fundamentals, technology, and applications* (William Andrew, 2015).
- [48] I. Fitis, M. Fakis, I. Polyzos, V. Giannetas, and P. Persephonis, "Two-photon polymerization of a diacrylate using fluorene photoinitiators–sensitizers," *Journal of Photochemistry and Photobiology A: Chemistry* **215**, 25-30 (2010).

- [49] S. Dottermusch, D. Busko, M. Langenhorst, U. W. Paetzold, and B. S. Richards, "Exposure-dependent refractive index of Nanoscribe IP-Dip photoresist layers," *Opt. Lett.* **44**, 29-32 (2019).
- [50] J. Durisova, D. Pudis, M. Goraus, and P. Gaso, "IP-Dip photoresist surfaces for photonic applications prepared by laser lithography and studied by AFM," *Applied Surface Science* **461**, 108-112 (2018).
- [51] J. L. Digaum, J. J. Pazos, J. Chiles, J. D'Archangel, G. Padilla, A. Tatulian, R. C. Rumpf, S. Fathpour, G. D. Boreman, and S. M. Kuebler, "Tight control of light beams in photonic crystals with spatially-variant lattice orientation," *Opt. Express* **22**, 25788-25804 (2014).
- [52] C. Jain, A. Braun, J. Gargiulo, B. Jang, G. Li, H. Lehmann, S. A. Maier, and M. A. Schmidt, "Hollow core light cage: trapping light behind bars," *ACS Photonics* **6**, 649-658 (2018).
- [53] W. Liang, T. Wang, C. Yin, J. Dong, F. Leng, and H. Wang, "Super-broadband non-diffraction guiding modes in photonic crystals with elliptical rods," *J. Phys. D: Appl. Phys* **43**, 075103 (2010).
- [54] Y. Chuang and T. Suleski, "Photonic crystals for broadband, omnidirectional self-collimation," *J. Opt* **13**, 035103 (2011).
- [55] L. Jiang, H. Wu, and X. Li, "Polarization-insensitive and broad-angle self-collimation in a two-dimensional photonic crystal with rectangular air holes," *Appl. Opt.* **52**, 6676-6684 (2013).
- [56] R. E. Hamam, M. Ibanescu, S. G. Johnson, J. Joannopoulos, and M. Soljačić, "Broadband super-collimation in a hybrid photonic crystal structure," *Opt. Express* **17**, 8109-8118 (2009).
- [57] S. G. Johnson and J. D. Joannopoulos, "Block-iterative frequency-domain methods for Maxwell's equations in a planewave basis," *Opt. Express* **8**, 173-190 (2001).

- [58] R. C. Rumpf and J. J. Pazos, "Optimization of planar self-collimating photonic crystals," *J. Opt. Soc. Am. A* **30**, 1297-1304 (2013).
- [59] C. Xia, S. M. Kuebler, N. P. Martinez, M. Martinez, R. C. Rumpf, and J. Touma, "Wide-band self-collimation in a low-refractive-index hexagonal lattice," *Opt. Lett.* **46**, 2228-2231 (2021).
- [60] J. C. Maxwell-Garnett, "Colours in metal glasses and in metallic films," *Philos. Trans. R. Soc. Lond. A* **203**, 385-420 (1904).
- [61] M. Noori, M. Soroosh, and H. Baghban, "Self-collimation in photonic crystals: applications and opportunities," *Ann. Phys.* **530**, 1700049 (2018).
- [62] B. Patiño-Jurado, J. F. Botero-Cadavid, and J. Garcia-Sucerquia, "Step-index optical fibers with 0.88 numerical aperture," *J. Light. Technol.* **37**, 3734-3739 (2019).
- [63] B. Oner, M. Turduev, and H. Kurt, "High-efficiency beam bending using graded photonic crystals," *Opt. Lett.* **38**, 1688-1690 (2013).
- [64] H. Kurt, E. Colak, O. Cakmak, H. Caglayan, and E. Ozbay, "The focusing effect of graded index photonic crystals," *Appl. Phys. Lett.* **93**, 171108 (2008).
- [65] J. Moughames, S. Jradi, T. Chan, S. Akil, Y. Battie, A. E. Naciri, Z. Herro, S. Guenneau, S. Enoch, and L. Joly, "Wavelength-scale light concentrator made by direct 3D laser writing of polymer metamaterials," *Sci. Rep.* **6**, 1-8 (2016).
- [66] A. Martinez, H. Miguez, A. Griol, and J. Marti, "Experimental and theoretical analysis of the self-focusing of light by a photonic crystal lens," *Phys. Rev. B* **69**, 165119 (2004).

- [67] F. S. Roux and I. De Leon, "Planar photonic crystal gradient index lens, simulated with a finite difference time domain method," *Phys. Rev. B* **74**, 113103-113103 (2006).
- [68] E. Akmansoy, E. Centeno, K. Vynck, D. Cassagne, and J.-M. Lourtioz, "Graded photonic crystals curve the flow of light: An experimental demonstration by the mirage effect," *Appl. Phys. Lett.* **92**, 133501 (2008).
- [69] F. Gaufillet and E. Akmansoy, "Design and experimental evidence of a flat graded-index photonic crystal lens," *J. Appl. Phys* **114**, 083105 (2013).
- [70] Y. Y. Zhao, Y. L. Zhang, M. L. Zheng, X. Z. Dong, X. M. Duan, and Z. S. Zhao, "Three-dimensional Luneburg lens at optical frequencies," *Laser Photonics Rev.* **10**, 665-672 (2016).
- [71] B. H. Cumpston, S. P. Ananthavel, S. Barlow, D. L. Dyer, J. E. Ehrlich, L. L. Erskine, A. A. Heikal, S. M. Kuebler, I.-Y. S. Lee, and D. McCord-Maughon, "Two-photon polymerization initiators for three-dimensional optical data storage and microfabrication," *Nature* **398**, 51-54 (1999).
- [72] S. Sreenivasan, "Nanoimprint lithography steppers for volume fabrication of leading-edge semiconductor integrated circuits," *Microsyst. Nanoeng.* **3**, 1-19 (2017).
- [73] R. C. Rumpf and J. Pazos, "Synthesis of spatially variant lattices," *Opt. Express* **20**, 15263-15274 (2012).
- [74] A. Berrier, M. Swillo, N. Le Thomas, R. Houdré, and S. Anand, "Bloch mode excitation in two-dimensional photonic crystals imaged by Fourier optics," *Phys. Rev. B* **79**, 116-165 (2009).
- [75] J. Witzens and A. Scherer, "Efficient excitation of self-collimated beams and single Bloch modes in planar photonic crystals," *J. Opt. Soc. Am. A* **20**, 935-940 (2003).

- [76] A. F. Oskooi, D. Roundy, M. Ibanescu, P. Bermel, J. D. Joannopoulos, and S. G. Johnson, "MEEP: A flexible free-software package for electromagnetic simulations by the FDTD method," *Comput. Phys. Commun.* **181**, 687-702 (2010).
- [77] F. Schiappelli, R. Kumar, M. Prasciolu, D. Cojoc, S. Cabrini, M. De Vittorio, G. Visimberga, A. Gerardino, V. Degiorgio, and E. Di Fabrizio, "Efficient fiber-to-waveguide coupling by a lens on the end of the optical fiber fabricated by focused ion beam milling," *Microelectron. Eng.* **73**, 397-404 (2004).
- [78] S. A. Self, "Focusing of spherical Gaussian beams," *Appl. Opt.* **22**, 658-661 (1983).
- [79] J. M. Martin, "Coupling efficiency and alignment sensitivity of single mode optical fibers," Master's dissertation (University of Central Florida, 1979).
- [80] R. Brüning, Y. Zhang, M. McLaren, M. Duparré, and A. Forbes, "Overlap relation between free-space Laguerre Gaussian modes and step-index fiber modes," *J. Opt. Soc. Am. A* **32**, 1678-1682 (2015).
- [81] D. Lin, P. Fan, E. Hasman, and M. L. Brongersma, "Dielectric gradient metasurface optical elements," *Science* **345**, 298-302 (2014).
- [82] J. Trull, L. Maigyte, V. Mizeikis, M. Malinauskas, S. Juodkazis, C. Cojocar, M. Rutkauskas, M. Peckus, V. Sirutkaitis, and K. Staliunas, "Formation of collimated beams behind the woodpile photonic crystal," *Phys. Rev. A* **84**, 033812 (2011).
- [83] A. Taflove, S. C. Hagness, and M. Piket-May, "Computational electromagnetics: the finite-difference time-domain method," *The Electrical Engineering Handbook* **3**(2005).